Protonation/deprotonation-driven switch for the redox stability of low-potential [4Fe-4S] ferredoxin

Kei Wada[1,2,*], Kenji Kobayashi[3,†], Iori Era[4,†], Yusuke Isobe[3], Taigo Kamimura[4], Masaki Marukawa[1], Takayuki Nagae[5], Kazuki Honjo[4], Noriko Kaseda[1], Yumiko Motoyama[1], Kengo Inoue[6], Masakazu Sugishima[7], Katsuhiro Kusaka[8], Naomine Yano[9], Keiichi Fukuyama[10], Masaki Mishima[5], Yasutaka Kitagawa[4,*], Masaki Unno[3,10,*]

[1]Department of Medical Sciences, University of Miyazaki, Kiyotake, Miyazaki 889-1692, Japan,
[2]Frontier Science Research Center, University of Miyazaki, Kiyotake, Miyazaki 889-1692, Japan,
[3]Graduate School of Science and Engineering, Ibaraki University, Hitachi, Ibaraki 316-8511, Japan
[4]Graduate School of Engineering Science, Osaka University, Toyonaka, Osaka 560-8531, Japan
[5]Department of Molecular Biophysics, Tokyo University of Pharmacy and Life Sciences, Tokyo 192-0392, Japan.
[6]Department of Biochemistry and Applied Biosciences, Faculty of Agriculture, University of Miyazaki, Miyazaki 889-2192, Japan
[7]Department of Medical Biochemistry, Kurume University School of Medicine, Kurume, Fukuoka 830-0011, Japan
[8]Comprehensive Research Organization for Science and Society (CROSS) Neutron Science and Technology Center, Naka Ibaraki 319-1106, Japan
[9]Structural Biology Division, Japan Synchrotron Radiation Research Institute, Hyogo679-5198, Japan
[9]Graduate School of Science, Osaka University, Toyonaka, Osaka 560-0043, Japan
[10]Research and Education Center for Atomic Sciences Ibaraki University, Naka Ibaraki 319-1106, Japan

***Corresponding Authors**

Kei Wada *E-mail: keiwada@med.miyazak-u.ac.jp*

Yasutaka Kitagawa *E-mail: kitagawa.yasutaka.es@osaka-u.ac.jp*

Masaki Unno *E-mail: masaki.unno.19@vc.ibaraki.ac.jp*

Keywords

Iron-sulfur protein, neutron crystallography, density functional theory, redox potential

Footnote

[†]These authors contributed equally

Abstract

Ferredoxin is a small iron-sulfur protein and acts as an electron carrier. Low-potential ferredoxins harbor [4Fe-4S] cluster(s), which play(s) a crucial role as the redox center. Low-potential ferredoxins are able to cover a wide range of redox potentials (–700 to –200 mV); however, the mechanisms underlying the factors which control the redox potential are still enigmatic. Here, we determined the neutron structure of ferredoxin from *Bacillus thermoproteolyticus*, and experimentally revealed the exact hydrogen-bonding network involving the [4Fe-4S] cluster. The density functional theory calculations based on the hydrogen-bonding network revealed that protonation states of the sidechain of Asp64 close to the [4Fe-4S] cluster critically affected the stability of the reduced state in the cluster. These findings provide the first identification of the intrinsic control factor of redox potential for the [4Fe-4S] cluster in low-potential ferredoxins.

Introduction

Ferredoxin is known as a simple iron-sulfur (Fe-S) protein, and is ubiquitous in plants, animals, and prokaryotes(1, 2). Ferredoxins function as electron carriers for fundamental metabolic processes such as gluconeogenesis/glycolysis, photosynthesis, nitrogen fixation, and assimilation of hydrogens and sulfur species. Therefore, ferredoxins have a variety of redox partners. In photosynthetic organisms, ferredoxin receives an electron from photosystem I complex and serves as the electron donor for the reduction of $NADP^+$ (ferredoxin:$NADP^+$ oxidoreductase), pyruvate (pyruvate:ferredoxin oxidoreductase), nitrate (nitrate reductase), and sulfite (sulfite reductase) to generate sources of energy(3). In bacteria, oxidized ferredoxins are reduced *via* a reverse reaction such as by bacterial type ferredoxin:$NADP^+$ oxidoreductase and pyruvate:ferredoxin oxidoreductase, and electrons in the reduced ferredoxin are utilized by ferredoxin-dependent enzymes in various metabolism cascades(4).

Typical bacterial ferredoxin is a small protein consisting of approximately one hundred amino acid residues, primarily (approximately 20%) negatively charged residues, with an isoelectric point (pI) that is usually below pH 4.0. The ferredoxin also has four conserved cysteine residues to which the Fe-S cluster is ligated in most cases. The types of the cluster are known as the [4Fe-4S] types(5) (Fig.1). [4Fe-4S] ferredoxins may be further classified into low-potential and high-potential ferredoxins. Intriguingly, [4Fe-4S] ferredoxins exhibit a wide range of redox potentials while having the same form of the cluster in the active site(6). For instance, low-potential ferredoxins harboring [4Fe-4S] exhibit redox potentials typically ranging from –700 mV to –200 mV; in contrast, high-potential ferredoxins have redox potentials of +100 mV to +360 mV(7). Low-potential [4Fe-4S]

ferredoxins, which are typical bacterial-type ferredoxins, reduce most of the redox partners at physiological potentials, whereas high-potential ferredoxins called HiPIPs usually accept electrons from most redox partners. Notably, electron transfer events by low-potential [4Fe-4S] ferredoxins are remarkable reactions; the low-potential ferredoxin receives an electron and must maintain the reduced [4Fe-4S] cluster until it transfers the electron to the redox partner proteins. How the low-potential [4Fe-4S] cluster maintains stability in the reduced form is unknown. The surrounding environment of the [4Fe-4S] cluster must be conferred and controls electron competency/stability; however, the mechanism underlying the sophisticated regulation of the redox potential and electron flow are still elusive.

Computer simulations using model complexes of the Fe-S cluster showed that the covalent nature of the Fe-S cluster decreases due to hydrogen bonds with the surrounding amino acid residues, and the redox potential correlates well with the covalent nature(8). This indicates that the redox potential may be controlled by the hydrogen bonds between the main chain amide nitrogen and the sulfur in iron-sulfur clusters (NH...S). In contrast, Solomon and co-workers demonstrated the substantial influence of hydration, supplied by water molecules, on the variation in reactivity by X-ray absorption spectroscopy(9). The Fe-S covalency is much lower in natively hydrated [4Fe-4S] ferredoxin active sites but increases upon water removal. The density functional theory (DFT) calculations have supported a correlation between Fe-S covalency and ease of oxidation and therefore suggest that hydration accounts for most of the differences between ferredoxin redox potentials. However, the most critical problem in the computational calculations for the protein is that artificial

coordinates for hydrogen atoms, which are predicted and generated computationally, have been used thus far for the calculations.

The precise locations of the hydrogen atoms in proteins are difficult to determine experimentally because this requires high-resolution structural information. So far, the exceptional ultra-high-resolution structure at 0.48 Å for HiPIP from *Thermochromatium tepidum* has been reported by X-ray crystallography(10), and the details of the hydrogen bonding networks surrounding the [4Fe-4S] cluster were determined. Using the charge-density analysis focused the valence electron, and the iron 3*d* and sulfur 3*p* electrons of the high-potential (positivity potential) [4Fe-4S] cluster were visualized for the first time. This is currently the most accurate analysis of the protein structure, but few indications regarding the stability of the redox state of the [4Fe-4S] cluster were obtained. More recently, the neutron structure of the HiPIP has been reported, indicating that the orientation of the amide proton of Cys75, one of the ligand residues for the Fe-S cluster, was probably altered in the reduced and oxidized states, possibly because of the electron storage capacity of the iron-sulfur cluster(11).

The high-resolution structure of the low-potential [4Fe-4S] ferredoxin was reported using a gram-positive bacterium *Bacillus thermoproteolyticus* (*Bt*Fd). *Bt*Fd is a typical bacterial ferredoxin and is a small protein, a protein with pI in the acidic region, that consists of 81 residues and one [4Fe-4S] cluster (Fig. 1). The X-ray structure of *Bt*Fd has been reported at a 0.92 Å resolution(12), but the hydrogen atoms, particularly around the Fe-S clusters, could not be assigned on the electron density map. The DFT calculations, based on the *Bt*Fd structure, reported that the Fe-S covalencies of [4Fe-4S] clusters differ considerably from HiPIP because of hydrogen bonds with water molecules(9). In

112 this case, the hydrogen-bonding networks surrounding the Fe-S clusters also used the putative
113 positions based on the calculations.

114 Neutron crystallography is a powerful analytic method because the hydrogen atoms can be
115 visualized and the radiation damage is negligible. In this study, we proceeded to experimentally
116 visualize the hydrogen bonds around the oxidized [4Fe-4S] cluster in *Bt*Fd by neutron crystal structure
117 analysis under ambient air conditions and using the DFT method based on the experimentally
118 determined hydrogen bonding network. The DFT calculations revealed that the protonation states of
119 Asp64 located close to the reduced/oxidized [4Fe-4S] cluster significantly affected the redox stability
120 of the cluster. Furthermore, the autooxidation kinetics of the reduced [4Fe-4S] cluster of *Bt*Fd
121 prepared under anaerobic conditions supported the notion that Asp64 is critically involved in the
122 stability of the reduced [4Fe-4S] cluster. These findings provide the first identification of intrinsic
123 factors controlling the redox stability of the [4Fe-4S] cluster in low-potential ferredoxins.

124

125 **Results**

126 **Overall neutron structure of the low-potential [4Fe-4S] ferredoxin**

127 We have successfully determined the crystallization conditions of *Bt*Fd in which we could
128 obtain large crystals (>2 mm^3) using the dialysis method. The neutron structure of *Bt*Fd at room
129 temperature was refined to a 1.60 Å resolution. The *R*-factor and free *R*-factor were 16.7% and 18.4%,
130 respectively (Table 1). A total of 819 H/D atoms and 60 hydrating water molecules were identified
131 (Fig. 2A, Table 1, and Fig. S1). The overall structure was nearly identical to the previously reported
132 cryogenic X-ray structure (PDB ID: 1IQG) at 0.92 Å resolution, with a rms deviation of 0.16 Å for

Cα atoms when all residues (81 residues) were superimposed with least-squares fitting. Although the neutron-scattering length density map clearly shows the [4Fe-4S] cluster, the density for sulfur atoms was very low compared with most of the other atoms including the iron atoms (Fig. 2B). This is a reasonable result because the sulfur atom has a smaller neutron-scattering length b_c (10^{-12} cm) (^{32}S=0.2804) than other atoms (^{56}Fe=0.994, ^{12}C=0.6651, ^{14}N=0.937, ^{16}O=0.5803). The ability to clearly distinguish between iron atoms and sulfur atoms is one of the characteristics of neutron structure analysis. We also collected the X-ray diffraction data from the same crystal used for neutron diffraction intensity measurements, and the 1.45 Å resolution X-ray structure, obtained at room temperature, was also refined (Table 1). The electron density map of the [4Fe-4S] cluster showed the respective locations of iron and sulfur atoms with strong electron densities (Fig. 2C). Consequently, the joint refinement of the neutron structure with the X-ray structure gave the precise coordinates of the [4Fe-4S] cluster.

Hydrogen atoms around the low-potential [4Fe-4S] cluster

In the neutron structure, the hydrogen atoms around the [4Fe-4S] cluster were visualized, and the exact direction of hydrogen bonds could be determined (Fig. 2D and E). The Sγ of cysteine residues, as ligands of the [4Fe-4S] cluster, formed five hydrogen bonds with the main chain amino groups; Cys11-Sγ formed two hydrogen bonds with Ala13-NH and Ala33-NH, Cys14-Sγ bonded to Ala16-NH, and Cys61-Sγ bonded to Ile12-NH and Ser65-NH. In contrast, the Sγ of Cys17 formed no hydrogen bond. The sulfur in the [4Fe-4S] cluster also formed hydrogen bonds; [4Fe-4S]-S1 with Gly15-NH and [4Fe-4S]-S3 with Ile12-NH. In addition, we observed the hydrogen atom of the water

molecule (Water 237) close to the [4Fe-4S] cluster, which was bonded to [4Fe-4S]-S1 atom. In total, 9 hydrogen bonds were clearly identified around the [4Fe-4S] cluster (Fig. 2E). Nevertheless, the previously reported X-ray structure of [4Fe-4S] *Bt*Fd was at 0.92 Å resolution, and all of the hydrogen bonds were invisible. This demonstrated that neutron analysis is an indispensable method for determining the location of hydrogen atoms; the experimentally determined distances/angles are shown in Fig. 2E. Incidentally, depending on the bonding mode in which the S atom is bonded, if the S atom is a hydrogen bond acceptor, the -N-H…S hydrogen bond distance is estimated to be approximately 3.0 Å. In a special case known as an resonance-assisted H-bond, a -N-H…S distance of 2.44 Å has also been reported, in which case a strong hydrogen bond is formed(13). The average distance between the oxygen and the sulfur is reported to be 3.32 Å, and the distance of the nitrogen and sulfur is 10% longer compared to that of the oxygen and sulfur(13); the distance between the nitrogen and sulfur is estimated to be approximately 3.6–3.7 Å.

Importantly, the structural comparison showed that the neutron structure in this study was able to accurately revise the hydrogen network around the [4Fe-4S] cluster (Fig. 2F). The -OH group on the sidechain of Thr63 was located an appropriate distance from the [4Fe-4S] cluster in order to form a hydrogen bond. This group was thought to be hydrogen-bonded in previous X-ray study(12) as the hydrogen atom in this position was not visible, but the distance as well as the angle between the donor and acceptor atoms indicated the possibility of the formation of a sulfur-containing hydrogen bond(14). In the neutron crystal structure, Thr63-Oγ1 and the [4Fe-4S]-S4 atoms were also within the hydrogen-bonding distance (3.5 Å), however, the hydrogen atom identified pointed in a different direction from the iron-sulfur cluster, indicating that it did not form a hydrogen-bonding interaction

with the iron-sulfur cluster (Fig. 2F). Furthermore, the neutron-scattering length density clearly revealed hydrogen bonding to another residue; the sidechain of Thr63-Oγ1H and the main chain -CO of Thr10 clearly formed a hydrogen bond at a distance of 2.2 Å. In order to consider the redox potential, it is important to experimentally determine the exact hydrogen-bonding network, and, ultimately, a single hydrogen bond can make a critical difference.

Density functional theory calculations of the low-potential [4Fe-4S] cluster in *Bt*Fd

In this study, we were able to revise the hydrogen-bonding network around the low-potential [4Fe-4S] cluster. We then investigated the effect of hydrogen bonding around the active site by the DFT calculations using the [4Fe-4S] cluster model based on the neutron diffraction structure including some amino acid residues (**CM**), as shown in Fig. 3A. The Cartesian coordinates of the model are summarized in Table S1. At first, the charge/spin state of each iron atom in the [4Fe-4S] cluster was examined using a cluster model without amino acid (**CM$_{NA}$**) as shown in Fig. 3A. In accordance with previous reports(15, 16), the total energies of the 12 possible combinations of charge/spin alignments were examined for the [$Fe^{III}{}_2Fe^{II}{}_2$] (oxidized: *Ox*) and [$Fe^{III}Fe^{II}{}_3$] (reduced: *Red*) states as summarized in Table S2. As shown in Fig. 3B, the most stable spin alignments for the *Ox* and *Red* states are confirmed to be consistent with the states previously reported(16), thus we assumed those charge/spin alignments in the following calculations. Next, to estimate the effect of hydrogen bonding, the vertical ionization potential (IP) was estimated by the calculated energy gaps between oxidized [E(*Ox*)] and reduced [E(*Red*)] states(16, 17).

The calculated IP value of **CM** was –3.27 eV, suggesting the *Ox* state was 3.27 eV more stable

than the *Red* state in this structure. In order to consider the effect of the surrounding amino acids, the IP value was also calculated using $\mathbf{CM_{NA}}$. The calculated IP value was –4.15 eV, which was shifted 0.88 eV to the negative side in comparison with **CM**, suggesting that the surrounding amino acids affect the IP value. In the previous study(18), it was reported that [N–H ⋯ S] hydrogen bonds involved with the cluster stabilize the reduced state and shift the IP of the cluster to the positive side. Our result was, therefore, consistent with the previous study(18). However, a single [N–H ⋯ S] hydrogen bond is suggested to change the IP value approximately 0.3 eV(18), so the 0.88eV shift was much smaller than the value expected from the neutron structure (9 hydrogen bonds) around the active site. To explain this underestimation in the IP value, the lowest unoccupied molecular orbital (LUMO) of the oxidized state, which was the corresponding orbital in this redox reaction, was examined as illustrated in Fig. 3C. The LUMO was mainly localized around the 4Fe-4S cluster; however, unexpectedly appeared at the deprotonated Asp64. This means that the electron density is partially removed not only from the [4Fe-4S] cluster but also from Asp64 in the oxidation process (*Red* → *Ox*). We note that the carboxy group of Asp64 is not neutralized ($–COO^-$) in the neutron structure, but it is easily protonated and neutralized since Asp64 is on the surface of the protein. Therefore, the IP of the cluster was recalculated with the $\mathbf{CM_H}$ model as illustrated in Fig. 3A. Then the population of LUMO around Asp64 was removed and fully localized on the [4Fe-4S] cluster as illustrated in Fig. 3C. Interestingly, the calculated IP of $\mathbf{CM_H}$ (–1.06 eV) was largely shifted to the positive side in comparison with the deprotonated **CM**. The difference in the IP value between $\mathbf{CM_H}$ and $\mathbf{CM_{NA}}$ (3.09 eV) indicates a contribution of 0.34 eV per one hydrogen bond, which is comparable to the previous report(18). These results suggest that the protonation state of the sidechain of Asp64 plays important

roles for the stability of the reduced state, and furthermore in the control of electron transfer. To examine the charge difference between **CM** and $\mathbf{CM_H}$ in the simulation, we also constructed a new model including an additional OH^- ion around Asp64 ($\mathbf{CM_{HOH}}$) as illustrated in Fig. S2A. The total charge of the $\mathbf{CM_{HOH}}$ model corresponds to the **CM** model and includes the effect of the hydrogen bond. The calculated IP for the $\mathbf{CM_{HOH}}$ is –2.93 eV, therefore a contribution of a single hydrogen bond is 0.33 eV. This indicates that the relative stability of the *Red* state is suppressed compared with the $\mathbf{CM_H}$ but is significantly larger than the **CM**, suggesting the importance of the protonation of Asp64 (Fig. S2B).

To consider the effect of the structural change caused by the redox on the IP, geometrical optimization of the 4Fe-4S core was performed for the **CM** and $\mathbf{CM_H}$ models using the same level of theory to the single-point calculations. The optimized Cartesian coordinates are summarized in Table S3. As illustrated in Fig. S2A, the IP values of **CM** and $\mathbf{CM_H}$ change from –3.27 to –2.38 eV ($|\Delta IP|$ = 0.89 eV), and from –1.06 to –0.19 eV ($|\Delta IP|$ = 0.87 eV), respectively. These results indicate that the IP values are significantly affected by the structural rearrangement; however, the shifts ($|\Delta IP|$) are the same between the **CM** and $\mathbf{CM_H}$ models. In other words, the effect of the structural change on the redox in the IP value is important but the significance of the protonation to Asp64 is not changed, regardless of the structural rearrangement.

To consider the environmental effect of the surrounding protein, we also introduced The Polarizable Continuum Model (PCM) using the Integral Equation Formalism variant (IEFPCM) approximation. As summarized in Table S4 in detail, IP values of **CM** and $\mathbf{CM_H}$ becomes 1.62 eV and 2.59 eV, respectively, indicating that the environmental effect significantly changes the IP value.

On the other hand, a qualitative relationship between the IP values of the **CM** and **CM_H** models is not changed, although the difference in the IP values between **CM** and **CM_H** (ΔIP) is decreased from ca. 2.2 to 1.0 eV. From these results, we can conclude that the protein environment is essential for their IP values but does not change the relative difference between **CM** and **CM_H** (ΔIP) qualitatively.

The role of Asp64 in *Bt*Fd for the air-oxidation of the low-potential [4Fe-4S] cluster

The DFT calculations highlighted the influence of the Asp64 protonation state on the IP value of the [4Fe-4S] cluster. The IP value is directly reflected in the oxidation rate of the [4Fe-4S] cluster in atmospheric air, since the electron transfer rate to oxygen depends on the IP. In *Bt*Fd, the ultraviolet-visible (UV-Vis) spectra were changed between reduced and oxidized states of the [4Fe-4S] cluster (Fig. 4A); the absorption shoulders around 320 nm and 420 nm were increased by oxidation. Therefore, we prepared reduced *Bt*Fd under anaerobic conditions and measured the spectral changes at 420 nm, associated with air oxidation.

In wild-type *Bt*Fd, the time-dependent change of the UV-Vis spectrum is associated with oxidation of the [4Fe-4S] cluster and displayed typical Michaelis-Menten kinetics（Fig. 4B）. Therefore, we applied the global fitting to evaluate the oxidation rate (half time of maximum oxidation ($T_{1/2}$) as for the K_m in substrate affinity), and in the evaluation, small numbers indicated the fast oxidation reaction. Multiple measurements of the oxidation rates showed a $T_{1/2}$ of 100 sec for wild-type *Bt*Fd. In contrast, that of D64A-mutated *Bt*Fd was 166 sec, approximately 1.7 times slower than wild type. The D64N mutant also had a slow oxidation rate at 170 sec. These results clearly

258 indicate that a neutralizing mutation in Asp64 leads to a slow oxidation rate, and the reduced state of
259 the [4Fe-4S] cluster has greater stability than that of wild type.

260 *Bt*Fd has 15 aspartate residues including Asp64, all of which are located in the solvent-exposed
261 environment (Fig. 1). We mutated each aspartate to alanine and evaluated changes in oxidation rates;
262 however, only mutations in Asp64 resulted in oxidation rate changes (Fig. 4B and Fig. S3). *Bt*Fd also
263 has 5 glutamate residues, but none of these affected the oxidation rate (Fig. S3).

264 More interestingly, the D64N neutralizing mutation had the same effect on [4Fe-4S] as the D64A
265 mutation, and the D64R mutation, a positively charged mutant, also slowed the similar oxidation rate
266 (Fig. 4B). In contrast, the D64E mutation, a negatively charged mutation, did not affect the oxidation
267 rate. Namely, the carboxy group in this position exposed to solvent is indispensable for the function
268 of the electron transfer.

269

270 **The role of Asp64 in low-potential [4Fe-4S] *Bt*Fd for the redox potential**

271 To further evaluate the effect of the mutation, we determined the redox potential (E°, V versus
272 standard hydrogen electrode (SHE), pH 7.0 of each mutant by the cyclic voltammetry method; Fig.
273 4C). As a result, the redox potential of wild-type *Bt*Fd was estimated to be -346 mV. In contrast, the
274 potentials of the D64A and D64N-mutated *Bt*Fd were –276 mV and –286 mV, respectively. The
275 potential of the D64E mutation was –346 mV, similar to that of the wild type. The neutralizing
276 mutation in the Asp64 position causes the positive shift of 60 ~ 70 mV in redox potential. The
277 potential of the D64R mutation was estimated to be -307 mV, but its deviation is large (± 41.6 mV).

278

The effect of aspartate/glutamate residue in various ferredoxins harboring the low-potential [4Fe-4S] cluster

We performed further experiments to confirm whether the results obtained with *Bt*Fd are the same for various ferredoxins from different organisms. We attempted to overexpress and purify eight ferredoxins as in the phylogenetic tree (Fig. 5A) from Eukaryote, Archaea, and Bacteria, in which three of them were successfully obtained from the ferredoxins harboring the [4Fe-4S] or [3Fe-4S] cluster. The [4Fe-4S] ferredoxin from *Staphylococcus haemolyticus,* a close relative to *Bacillus thermoproteolyticus*, has an aspartate residue at the position of 65 (Fig. S4C), which corresponds to Asp64 in *Bt*Fd. The measurement of the air-oxidation rate indicated that the Asp65 mutation critically affected the rate as seen in that of *Bt*Fd (Fig. 5B). In the *Megalodesulfovirio* (*Desulfovibrio*) *gigas* [3Fe-4S] ferredoxin, the Glu53 is the corresponding position to the Asp64 in *Bt*Fd (Fig. S4C). The air-oxidation rate is quite slow and its rate is further slowed by introducing the E53A mutation (Fig. 5B). Surprisingly, even in the archaeal *Geoglobus acetivorans* [4Fe-4S] ferredoxin, which is phylogenetically quite distant from *Bt*Fd, the E56A mutation affected the oxidation rate (Fig. 5B).

Discussion

Redox potentials are major contributors to controlling electron transfer rates and thus regulating electron transfer processes in biological reactions. Elucidating how proteins control the redox potentials of Fe–S clusters is a longstanding fundamental question. Possible controlling factors that have been proposed as being important include the solvent exposure of the cluster, specific hydrogen-bonding networks, especially NH…S bonds, and the proximity and orientation of the protein

300 backbone and sidechain dipoles.(7, 19-22) Thus far, several mutagenesis studies have demonstrated
301 that the redox potential of ferredoxin can be changed by introducing artificial mutations into residues
302 near Fe-S clusters. For instance, in [4Fe-4S] ferredoxin from *Azotobacter vinelandii* (*Av*Fd I),
303 mutations in positions Phe2 or Phe25 showed a large shift (100–200 mV versus SHE) in reduction
304 potentials(23). The series of mutations based on the sequence/structural comparison among *Av*Fd I
305 and *Peptostreptococcus asaccharolyticus* ferredoxin (*Pa*Fd) and related ferredoxins showed that three
306 mutations, V19E, P47S, and L44S in *Av*Fd I also shift to higher reduction potentials (130 mV
307 increasing in total)(19). These artificial mutation studies clearly showed the significance of the
308 environment of [4Fe-4S] for redox potentials; however, their intrinsic control residues have remained
309 ambiguous.

310 In this study, we showed that Asp64 in the *Bt*Fd affected the behaviors of the [4Fe-4S] cluster
311 including the redox potential (Fig. 4B and C). During the course of the purification, all of the mutated
312 *Bt*Fd eluted at the same conductivity from the high-resolution ion-exchange column, that is, the
313 aspartate mutation in various positions did not disturb the net charge of this protein. Also, the
314 respective UV-Vis spectra of the reduced and oxidized forms of *Bt*Fd mutants were the same as that
315 of the wild type (Fig. S4), demonstrating that the environment of the [4Fe-4S] cluster was not altered
316 by these mutations. These results indicated that the acidic residue mutations in other positions did not
317 significantly affect the oxidation rate (Fig. 4B). The distances between the Asp/Glu and [4Fe-4S]
318 cluster are listed in Table S5; the sidechain of Asp64 is located at 10.1 Å, and the Asp7 (10.5 Å),
319 Asp26 (12.0 Å), Asp28 (11.3 Å), Asp30 (13.7 Å), Asp53 (13.7 Å), Glu9 (13.7 Å), and Glu59 (12.8
320 Å) were located at similar distances. Taken together, only Asp64 affects the oxidation rate of the

321 [4Fe-4S] cluster, and the protonation state of Asp64 directly contributes to the control of electron
322 potential of the [4Fe-4S] cluster.

323 The mutation experiments showed that the Asp64 residue in *Bt*Fd was exchangeable with a
324 glutamate residue, which means that the carboxy group in this position is indispensable. The sequence
325 alignment of the low-potential [4Fe-4S] ferredoxin demonstrated that negatively charged residues,
326 aspartate or glutamate, are highly conserved at this position among low-potential [4Fe-4S]
327 ferredoxins in bacteria (Fig. S6). Interestingly, the significance of the highly conserved aspartate or
328 glutamate was demonstrated for the ferredoxins from different organisms even in organisms distantly
329 related in the evolutionary phylogenetic tree (Fig. 5A and B). That is, the effect of the D64A mutation
330 in the [4Fe-4S] *Bt*Fd in gram-positive bacteria is also observed in the E56A mutation and in archaeal
331 [4Fe-4S] ferredoxin from *Geoglobus acetivorancs*. Furthermore, the same results are obtained from
332 the [4Fe-3S] ferredoxin from *Megalodesulfovibrio gigas,* a gram-negative bacterium. Thus, the
333 control mechanism of the redox-state stability found in *Bt*Fd may be a common mechanism, at least
334 in low-potential [4Fe-4S] and [3Fe-4S] ferredoxins.

335 In general, the p*K*a value of the aspartic acid sidechain is a pH of approximately 3.9, meaning
336 that under physiological conditions, the sidechain of Asp64 is constantly in a deprotonated state. We
337 have attempted to determine the p*K*a value of the Asp64 in *Bt*Fd by monitoring the chemical shifts of
338 the Asp64 sidechain ^{13}CO(γ) using nuclear magnetic resonance to determine the pH titration of Asp64.
339 Under the reduced conditions we could not determine the p*K*a value of the carboxylate hampering the
340 paramagnetic property of the reduced [4Fe-4S] cluster. Instead, under the oxidative conditions
341 (normal ambient air conditions), the p*K*a of Asp64 was successfully estimated to be approximately

342 4.9 (Fig. S7A and B, SI method and text). This indicated that the p*K*a of Asp64 shifted to neutral. To
343 further estimate the p*K*a under reduced conditions, we applied the air-oxidation measurement; the
344 oxidation rate of the wild-type *Bt*Fd changed dramatically between pH 6.0 to 7.0 (Fig. S7C). In
345 contrast the D64A *Bt*Fd did not alter the rate according to the pH. These results indicate that the p*K*a
346 value of Asp64 is thought to be between a pH of 6.0 to 7.0. The [4Fe-4S] cluster in the *Bt*Fd was
347 stable enough to conduct these experiments under acidic to basic conditions (pH 4.5–9.0) (Fig. S8).
348 Thus, the protonation/deprotonation of Asp64 likely occurs even in physiological conditions.

349 The structural basis of the interactions between ferredoxin and its partner proteins has been
350 previously reported(24-26). In the reported structures, ferredoxins bound to their partner proteins such
351 as ferredoxin:$NADP^+$ oxidoreductase or photosystem I were required to directly face the Fe-S cluster
352 region to effectively accept electrons from their partner proteins. These complex structures are
353 derived from photosynthetic organisms, and ferredoxins harboring a [2Fe-2S] cluster are called plant-
354 type ferredoxins. Unfortunately, there is no structural report about the characteristics of the interaction
355 between bacterial [4Fe-4S] ferredoxins and their partner proteins, although the major interaction
356 region of ferredoxin must be in close contact with the Fe-S cluster. In bacterial low-potential [4Fe-
357 4S] ferredoxins, if an aspartate residue neighboring the [4Fe-4S] cluster, corresponding to Asp64 in
358 *Bt*Fd, was protonated by complex formation, electrons received from the bacterial ferredoxin:$NADP^+$
359 oxidoreductase complex are able to remain stable. According to the Frank-Condon principle, known
360 as the ground rule of the electron transfer, the electronic transitions are relatively instantaneous
361 compared with the time scale of nuclear motions. As well, in *Bt*Fd, the distance between the [4Fe-4S]
362 cluster and the carboxy sidechain of Asp64 was close enough to enable the electron transfer as the

363 corresponding distance is approximately 10 Å (Table S5). Therefore, the protonation state of the
364 aspartate residue neighboring the [4Fe-4S]/[3Fe-4S] cluster is a reasonable switch to control the
365 stability of the reduced state in the [4Fe-4S]/[3Fe-4S] cluster. We propose a control mechanism of
366 the redox potential in low-potential [4Fe-4S]/[3Fe-4S] ferredoxins as shown in Fig. S9. This
367 protonation-driven switch is likely reasonable to prevent the backflow of accepted electrons.

368 To our knowledge, this is the first proposed mechanism of the intrinsic control factor of redox
369 potentials of the [4Fe-4S]/[3Fe-4S] cluster in low-potential ferredoxins. We hope that the
370 determination of complex structures with electron donors and acceptors involving ferredoxin will
371 elucidate more detailed control mechanisms for electron transfer by low-potential [4Fe-4S]/[3Fe-4S]
372 ferredoxins.

373

374 ## Materials and Methods

375 **Expression and purification of the low-potential ferredoxin of [4Fe-4S] *Bt*Fd**

376 Expression and purification of [4Fe-4S] *Bt*Fd were conducted as previously reported(12, 27), with
377 some modifications. The plasmid pET-21a(+)-*btfd* gene was co-expressed with the *isc* operon (pRK-
378 ISC)(28) in the *E. coli* strain C41(DE3) to produce holo-*Bt*Fd in high yield. The bacteria were
379 cultivated in 2.5 liters of Terrific broth containing 100 μg/mL ampicillin, 5 μg/mL tetracycline, and
380 0.1 mg/mL ferric ammonium citrate. Expression was induced with 0.5 mM IPTG and the cells were
381 further grown for 20 h at 28°C. The cells were disrupted by sonication, and the suspension was
382 centrifuged at 12,000 *g* for 30 min at 4°C. The colored supernatant was subjected to ammonium
383 sulfate fractionation at 60% saturation. After centrifugation, the supernatant fraction was applied to

384 HiPrep Butyl FF 16/10 (Cytiva, Marlborough, MA, USA) and eluted with a linear gradient of
385 ammonium sulfate (5–25%) in 50 mM Tris-HCl, pH 7.8. The grayish brown fractions were dialyzed
386 against a solution containing 50 mM Tris-HCl, pH 7.8, applied to an anion exchange column (Mono
387 Q HR 5/5, Cytiva) chromatography using the NGC Quest 10 system (Bio-Rad Laboratories, Inc.
388 Hercules, CA).
389

390 **Expression and purification of the low-potential ferredoxin of [4Fe-4S], [4Fe-4S]x2, and [3Fe-**
391 **4S] ferredoxin from various organisms**

392 Expressions and purifications of [4Fe-4S] ferredoxins were conducted using the same procedures as
393 that of *Bt*Fd. Each ferredoxin gene was constructed using a synthetic oligonucleotide (Eurofins Japan,
394 Tokyo) based on UniProt database sequence optimized for the *E. coli* codon usage.
395

396 **Crystallization of [4Fe-4Fe] BtFd for neutron crystallography**

397 The crystallization procedure and conditions are as follows and were modified from the method
398 reported previously to grow large crystals for neutron crystallography(12). Purified [4Fe-4S] BtFd
399 was concentrated by centrifugation using an Amicon Ultra centrifugal filter unit 3K (Merck
400 Millipore) to 30–40 mg/mL. The crystal for the neutron diffraction experiment was obtained with the
401 dialysis method at 4°C using a 50 μL dialysis button (Hampton Research, Journey Aliso Viejo, CA,
402 USA) and the excess amount of the reservoir solution containing 200 mM NaCl, 1.4 M ammonium
403 sulfate, and 50 mM MES (pH 5.9). The crystal appeared within one month and was grown to
404 approximately 2.5 mm × 1.8 mm × 0.6 mm in a month.

Neutron diffraction experiment. The crystal was soaked to 50 μL of 50 mM MES buffer (pD 6.3) containing 200 mM NaCl and 1.4 M ammonium-d8 sulfate (D8, 98%; Cambridge Isotope Laboratories Inc.) prior to the neutron diffraction experiment. The soaking solution was exchanged three times in three weeks. The crystal was mounted in a quartz glass capillary with 3.5 mm ϕ and 0.01 mm thickness (Hilgenberg). Inside the capillary, a small amount of deuterated reservoir solution was contained to avoid drying up the crystal, and the capillary was sealed with epoxy resin. Time-of-flight (TOF) neutron diffraction data were collected at BL03 iBIX (29) in a Japan Proton Accelerator Research Complex (J-PARC, Tokai, Japan) at room temperature. Thirty-two wavelength-shifting fiber-based scintillator neutron detectors with a surface area of 133 mm × 133 mm were used to collect the data. A total of 56 data sets were collected using a wavelength of 1.5–4.5 Å with a detector distance of 490 mm. Exposure time for each data set was 6 h at 500 kW of the J-PARC accelerator power. The TOF neutron data were indexed, integrated, scaled, and processed with STARGazer(30). The neutron diffraction data statistics are listed in Table 1.

X-ray diffraction experiment. X-ray diffraction data from the same crystal used for neutron crystallography were collected using an ADSC Quantum270 CCD detector at NW12A in Photon Factory Advanced Ring (PF-AR; Tsukuba, Japan) under room temperature. The wavelength of the synchrotron radiation, transmittance, and slit size were 1.000 Å, 1%, and 0.20 mm (horizontal) × 0.05 mm (vertical), respectively.[31] The sample-to-detector distance, oscillation range and exposure time were 75 mm, 0.5° and 0.5 sec, respectively. In total, 720 images were collected. Data were integrated, merged, and processed with HKL-2000(31). The X-ray diffraction data collection and statistics are listed in Table 1.

429 **Structure refinement.** The structure was determined by molecular replacement method using the
430 previously determined X-ray structure of [4Fe-4S] *Bt*Fd (PDB ID: 1IQZ) from which the waters and
431 [4Fe-4S] cluster were removed as the initial model. The first refinement was carried out using the
432 rigid-body refinement program RefMac5(32) from 8.0 to 3.0 Å resolution range using only X-ray
433 intensity data. The *R* factor was dramatically dropped by rigid-body refinement. Then, the joint
434 refinement was carried out with both the neutron and X-ray diffraction data using PHENIX(33). The
435 1.6 Å resolution neutron data and the 1.45 Å resolution X-ray data were used for the structure
436 refinement. Five percent of the data were selected by PHENIX for cross-validation. The neutron
437 scattering length density and electron density maps were visualized and manual model refinement
438 was carried out using COOT(34). Protonation states of amino acid residues and orientation of water
439 molecules were manually adjusted by watching both the neutron scattering length density and electron
440 density calculated before including the hydrogens (H)/deuteriums (D) on COOT; only the neutron
441 scattering length density appeared for the positions of the H (negative density)/D (positive density)
442 atoms. The temperature factors for all atoms and occupancies for H/D atoms and residues having dual
443 conformations were also refined. The refinement statistics are also listed in Table 1. All structure
444 illustrations in figures except for Fig. 3 were prepared with Pymol(35).
445
446 **DFT calculations** All calculations were performed by using the spin-unrestricted hybrid DFT method
447 with the B3LYP functional set. As the basis set, 6-31G* and 6-31+G* were used for [Fe, C, N, O, H]
448 and [S] atoms, respectively, for the IP calculations. Only the position of a hydrogen atom bound to a
449 carboxy group of Asp64 in CM_H was optimized using the 6-31G [Fe, C, H], 6-31G* [N, O], and 6-

31+G* [S] basis sets while the other atoms remained fixed. All of these calculations were carried out in gas phase conditions using the Gaussian 09 program package(36).

The IP was defined as the vertical ionization potential values of the reduced state calculated by IP $=E(Ox)–E(Red)$, where $E(Ox)$ and $E(Red)$ were calculated as total energies of the oxidized (*Ox*) and reduced (*Red*) states by the DFT method(16, 17).

Cartesian coordinates of calculated models are summarized in Table S1. From the formal charges of Fe, S and other ligands, we assumed that the total charges of the $\mathbf{CM_{NA}}$ and **CM** models are –3 and –4 for oxidized (*Ox*) and reduced (*Red*) states, respectively, whilst total charges are –2 and –3 for the *Ox* and *Red* models in the case of the $\mathbf{CM_{H}}$ model. The $\mathbf{CM_{HOH}}$ model is constructed by placing the OH^- ion close to Asp64 in the initial structure, followed by a geometric optimization of only the OH^- fragment for both the reduced and oxidized states. To examine the effect of the OH^- in detail, the OH^- fragment is moved along the O–H axis of the OH^- fragment in 0.5Å step. The spin states of *Ox* and *Red* states are the open-shell singlet and doublet states, respectively. The calculated Mulliken charges and spin densities of [4Fe-4S] cores are added in Table S2. As mentioned in the main text, the most stable spin/charge alignment of Fe ions were examined among 12 possible spin/charge combinations using **CM** model, and all other following calculations were only assumed to be these ground states (see Table S2A and B). It is reported that the molecular charges sometimes cause the error especially under approximation of the solvation effect by PCM(37), however the simulation is performed in the gas phase, therefore such effect is assumed to be negligible.

470 **Oxidation rate analysis of [4Fe-4S] *Bt*Fd and its mutated proteins.** Site-directed mutagenesis was
471 carried out using a KOD -plus- Mutagenesis Kit (Toyobo), with a pET21a(+)-containing *Bt*Fd gene
472 as a template. Sequence analysis verified that the resultant constructs were free of errors. Expression
473 and purification of mutated [4Fe-4S] *Bt*Fds were performed in the same way as that for wild type.
474 Prior to the oxidation rate measurement, we performed a complete reduction of [4Fe-4S] *Bt*Fd by
475 using dithionite; 1 mM (final concentration) dithionite was added to 100 μL of [4Fe-4S] *Bt*Fd (6.0
476 mg/ml) in anaerobic conditions (O_2 < 5 ppm; COY). After 1 h of incubation at 4 °C, the dithionite
477 was removed by size-exclusion chromatography (HiTrap Desalting 5 ml column; Cytiva) equipped
478 with the AKTA START system under anaerobic conditions. Complete removal of the dithionite was
479 able to be confirmed with the chromatogram, which indicated the two separated peaks derived from
480 the reduced [4Fe-4S] *Bt*Fd and dithionite. The fraction containing reduced [4Fe-4S] *Bt*Fd (1 mL) was
481 moved into quartz cells with the screwcap under anerobic conditions, and taken out of the anaerobic
482 chamber. Then, the UV-Vis spectroscopic measurement (V730BIO, JASCO) was started immediately
483 after the screwcap was opened. The spectral changes at 420 nm were measured every second for 10
484 mins, and the measurements were performed three times, at least for the global fitting. The
485 temperature of the cell chamber in the spectrometer was strictly controlled at 28 °C by the Peltier
486 water-cooled cell-holder and the cell solution was continuously mixed by a micro-stirrer. The global
487 fittings of the Michaelis-Menten curve were performed using the kinetics curve fitting mode in the
488 GraphPad Prism 9 (GraphPad Software, San Diego, CA USA, www.graphpad.com).
489

490 **The electrochemical measurement of [4Fe-4S] *Bt*Fd and its mutated proteins.** To exchange the
491 buffer, the purified *Bt*Fd and its mutated proteins were precipitated by ammonium sulfate and the
492 precipitate was suspended in the buffer at various pHs; the sample solutions contained 100 μM *Bt*Fd,
493 625 mM NaCl, 2.5 mM neomycin, and 50 mM Tris-HCl at a pH of 7.8 or 50 mM MES-Tris mixed
494 buffer at a pH of 6.0–9.0. The cyclic voltammetry was performed using the μStat-I 400 bipotentiostat
495 (Metrohm AG, Switzerland) controlled by Drop-View 8400 software. A disposable screen-printed
496 carbon electrode (DRP-110, Metrohm AG) was formed by a carbon ink and acted as a working
497 electrode (4 mm diameter). Voltammetric measurements used Ag as a pseudo-reference electrode and
498 carbon ink as a counter electrode. Five cyclic scans were recorded between −0.80 and –0.40 V at a
499 0.05 V s^{-1} sweep rate. The CV measurements were performed anaerobically by setting the devices,
500 including the potentiostat and the disposable electrode, in an anaerobic chamber (O_2 < 5 ppm; COY).

501

502 **Data availability**

503 The atomic coordinates and structure factors for the neutron structure of the *Bt*Fd at room temperature
504 have been deposited in the PDB under accession code 7YL8.

505

506 **Acknowledgements**

507 We would like to express our deepest appreciation to Research Fellows Ms. Makiko Ishihara and
508 Dr. Kenji Ite for their many suggestions and advice. We thank Dr. Yu Hirano of the Institute for
509 Quantum Life Science for the helpful advice on the neutron crystal structure analysis. We also thank

members of iBIX at J-PARC of Japan for the neutron diffraction data collection. The neutron diffraction experiments, including the test experiments, were conducted under Proposals 2016PX0003, 2017PX0004, 2019PX3020, and 2020PX3006 (Ibaraki Prefecture Project) in J-PARC. We thank members of the Structural Biology beamlines of PF and SPring-8 for the X-ray diffraction data collection, including preliminary experiments. The X-ray diffraction experiments were conducted under Proposals 2017G561 and 2019G512 in PF and 2022A2724 in SPring-8. This work was partly supported by JSPS KAKENHI numbers 23K17981 (to K.W.), 21H5260 (to K.W.), 20H03196 (to K.W.), 16K07261 (to M.U.), 21K05016 (to S.M.), 22H02562 (to M.M.), 21H01951(to Y.K), 22H02050 (to Y.K.), Ibaraki Prefecture's Sendokenkyu from 2016 to 2021 (to M.U.), The Takeda Science Foundation (to K.W.) and the Japan Foundation for Applied Enzymology (to K.W.). This research was partially supported by Research Support Project for Life Science and Drug Discovery (Basis for Supporting Innovative Drug Discovery and Life Science Research (BINDS)) from AMED and the Frontier Science Research Center, University of Miyazaki. We also thank T. Yokoyama, T. Kawaguchi, A. Yoshida and Y. Kawagoe of the University of Miyazaki for technical assistance.

Author contributions: K.F., K.W and M.U. initiated and directed this study together with Y.K., M.M. K.W, K.K Y.I. and M.M prepared proteins. K.K., Y.I., K.K, N.Y and M.U. performed neutron and/or X-ray structural biology experiments. I.E., T.K. and Y.K. performed computational studies of the DFT calculations. M.M., K.I, M.S, K.F. and K.W performed the biological experiments. All authors participate in the data analysis and manuscript preparation.

Competing interests: The authors declare no competing interest.

References

1. R. Lill, J. B. Broderick, D. R. Dean, Special issue on iron-sulfur proteins: Structure, function, biogenesis and diseases. *Biochim Biophys Acta* **1853**, 1251-1252 (2015).
2. H. Matsubara, Y. Katsube, K. Wada, *Iron-sulfur protein research* (Japan Scientific Societyes Press, Springer-Verlag, Tokyo, 1987).
3. J. J. Pierella Karlusich, N. Carrillo, Evolution of the acceptor side of photosystem I: ferredoxin, flavodoxin, and ferredoxin-$NADP^+$ oxidoreductase. *Photosynth Res* **134**, 235-250 (2017).
4. R. C. Valentine, Bacterial Ferredoxin. *Bacteriol Rev* **28**, 497-517 (1964).
5. J. Meyer, Iron-sulfur protein folds, iron-sulfur chemistry, and evolution. *J Biol Inorg Chem* **13**, 157-170 (2008).
6. H. Beinert, R. H. Holm, E. Munck, Iron-sulfur clusters: nature's modular, multipurpose structures. *Science* **277**, 653-659 (1997).
7. P. Hosseinzadeh, Y. Lu, Design and fine-tuning redox potentials of metalloproteins involved in electron transfer in bioenergetics. *Biochim Biophys Acta* **1857**, 557-581 (2016).
8. E. Adman, K. D. Watenpaugh, L. H. Jensen, NH---S hydrogen bonds in *Peptococcus aerogenes* ferredoxin, *Clostridium pasteurianum* rubredoxin, and Chromatium high potential iron protein. *Proc Natl Acad Sci U S A* **72**, 4854-4858 (1975).
9. A. Dey *et al.*, Solvent tuning of electrochemical potentials in the active sites of HiPIP versus ferredoxin. *Science* **318**, 1464-1468 (2007).
10. Y. Hirano, K. Takeda, K. Miki, Charge-density analysis of an iron-sulfur protein at an ultra-high resolution of 0.48 Å. *Nature* **534**, 281-284 (2016).
11. Y. Hanazono *et al.*, Revisiting the concept of peptide bond planarity in an iron-sulfur protein by neutron structure analysis. *Sci Adv* **8**, eabn2276 (2022).
12. K. Fukuyama, T. Okada, Y. Kakuta, Y. Takahashi, Atomic resolution structures of oxidized [4Fe-4S] ferredoxin from *Bacillus thermoproteolyticus* in two crystal forms: systematic distortion of [4Fe-4S] cluster in the protein. *J Mol Biol* **315**, 1155-1166 (2002).

13. G. Gilli, P. Gilli, *The Nature of the Hydrogen Bond. Outline of a Comprehensive Hydrogen Bond Theory* (Oxford University Press Oxford, 2009).
14. P. Zhou, F. Tian, F. Lv, Z. Shang, Geometric characteristics of hydrogen bonds involving sulfur atoms in proteins. *Proteins* **76**, 151-163 (2009).
15. Y. Kitagawa *et al.*, Theoretical studies on effects of hydrogen bonds attaching to cysteine ligands on 4Fe-4S clusters. *Int. J. Quant. Chem.* **108**, 2881-2887 (2008).
16. R. A. Torres, T. Lovell, L. Noodleman, D. A. Case, Density functional and reduction potential calculations of Fe_4S_4 clusters. *J Am Chem Soc* **125**, 1923-1936 (2003).
17. J. M. Mouesca, J. L. Chen, L. Noodleman, D. Bashford, D. A. Case, Density Functional/Poisson-Boltzmann Calculations of Redox Potentials for Iron-Sulfur Clusters. *J. Am. Chem. Soc.* **116**, 11898–11914 (1994).
18. I. Era *et al.*, Theoretical Study on Redox Potential Control of Iron-Sulfur Cluster by Hydrogen Bonds: A Possibility of Redox Potential Programming. *Molecules* **26** (2021).
19. K. Chen *et al.*, *Azotobacter vinelandii* ferredoxin I: a sequence and structure comparison approach to alteration of $[4Fe\text{-}4S]^{2+/+}$ reduction potential. *J Biol Chem* **277**, 5603-5610 (2002).
20. B. Shen *et al.*, *Azotobacter vinelandii* ferredoxin I. Alteration of individual surface charges and the $[4FE\text{-}4S]^{2+/+}$ cluster reduction potential. *J Biol Chem* **269**, 8564-8575 (1994).
21. R. Langen, G. M. Jensen, U. Jacob, P. J. Stephens, A. Warshel, Protein control of iron-sulfur cluster redox potentials. *J Biol Chem* **267**, 25625-25627 (1992).
22. G. R. Moore, G. W. Pettigrew, N. K. Rogers, Factors influencing redox potentials of electron transfer proteins. *Proc Natl Acad Sci U S A* **83**, 4998-4999 (1986).
23. K. Chen *et al.*, Crystal structures of ferredoxin variants exhibiting large changes in [Fe-S] reduction potential. *Nat Struct Biol* **9**, 188-192 (2002).
24. I. Caspy, A. Borovikova-Sheinker, D. Klaiman, Y. Shkolnisky, N. Nelson, The structure of a triple complex of plant photosystem I with ferredoxin and plastocyanin. *Nat Plants* **6**, 1300-1305 (2020).
25. H. Kubota-Kawai *et al.*, X-ray structure of an asymmetrical trimeric ferredoxin-photosystem I complex. *Nat Plants* **4**, 218-224 (2018).
26. G. Kurisu *et al.*, Structure of the electron transfer complex between ferredoxin and ferredoxin-$NADP^+$ reductase. *Nat Struct Biol* **8**, 117-121 (2001).

27. T. Shirakawa *et al.*, Identification of variant molecules of *Bacillus thermoproteolyticus* ferredoxin: crystal structure reveals bound coenzyme A and an unexpected [3Fe-4S] cluster associated with a canonical [4Fe-4S] ligand motif. *Biochemistry* **44**, 12402-12410 (2005).
28. U. Tokumoto, Y. Takahashi, Genetic analysis of the *isc* operon in *Escherichia coli* involved in the biogenesis of cellular iron-sulfur proteins. *J Biochem* **130**, 63-71 (2001).
29. I. Tanaka *et al.*, Neutron structure analysis using the IBARAKI biological crystal diffractometer (iBIX) at J-PARC. *Acta crystallographica. Section D, Biological crystallography* **66**, 1194-1197 (2010).
30. T. Ohhara *et al.*, Development of data processing software for a new TOF single crystal neutron diffractometer at J-PARC. *Nuclear Instruments and Methods in Physics Research Section A: Accelerators, Spectrometers, Detectors and Associated Equipment* **600**, 195-197 (2009).
31. Z. Otwinowski, W. Minor, "Processing of X-ray diffraction data collected in oscillation mode" in Methods in Enzymology, J. C.W. Carter, R. M. Sweet, Eds. (Academic Press New York, 1997), vol. 276, pp. 307-326.
32. G. N. Murshudov *et al.*, REFMAC5 for the refinement of macromolecular crystal structures. *Acta Crystallogr D Biol Crystallogr* **67**, 355-367 (2011).
33. P. D. Adams *et al.*, PHENIX: a comprehensive Python-based system for macromolecular structure solution. *Acta crystallographica. Section D, Biological crystallography* **66**, 213-221 (2010).
34. P. Emsley, K. Cowtan, Coot: model-building tools for molecular graphics. *Acta crystallographica. Section D, Biological crystallography* **60**, 2126-2132 (2004).
35. W. L. DeLano, *The PyMOL Molecluar Graphics System*, DeLano Scientific LLC, San Carlos, CA (2002).
36. M. J. Frisch *et al.*, Gaussian 09 Rev.C01. *Gaussian Inc., Wallingford,* , CT, USA (2009).
37. T. Matsui, Y. Kitagawa, Y. Shigeta, M. Okumura, A Density Functional Theory Based Protocol to Compute the Redox Potential of Transition Metal Complex with the Correction of Pseudo-Counterion: General Theory and Applications. *J Chem Theory Comput* **9**, 2974-2980 (2013).

Figure legends

Fig. 1 Ternary and primary structures of low-potential [4Fe-4S] *Bt*Fd.

(*A*) The 3D structure of BtFd (PDB id: 1IQZ). The [4Fe-4S] cluster and aspartate residues are shown as a space-filling model, and the ligand cysteines for the Fe-S cluster are shown as yellow sticks. The surface drawing is superposed on the cartoon model. (*B*) Whole amino acid sequence of BtFd. The ligating manner of the [4Fe-4S] cluster is illustrated, and the ligand cysteine and aspartate residues are highlighted.

Fig. 2 Neutron structure of low-potential [4Fe-4S] *Bt*Fd

(*A*) Overall neutron structure of *Bt*Fd. *Bt*Fd polypeptides are colored in rainbow colors from blue (N-terminus) to red (C-terminus). The [4Fe-4S] cluster and water molecules are shown as a space-filling model. White and cyan balls indicate hydrogen (deuterium) and oxygen atoms, respectively. The figure on the right is the left one rotated approximately 90°. (*B*) The $2F_o$–F_c (1.0 sigma: blue cage) and F_o–F_c (3.0 sigma: green cage) neutron-scattering length density map around the [4Fe-4S] cluster and the structural model. The $2F_o$–F_c map is shown within 1 Å around the [4Fe-4S] cluster for clarity. (*C*) X-ray electron density map of the corresponding region of (*B)*. $2F_o$–F_c (5.0 sigma) and F_o–F_c (3.0 sigma) maps are shown in blue and green, respectively. (*D*) Hydrogen bond with the [4Fe-4S] cluster and its ligand Sγ atoms of cysteines. The hydrogen (deuterium), oxygen, carbon, and nitrogen atoms are shown in white, red, cyan, and blue, respectively. The hydrogen bonds indicate pink broken lines and the distance between the amide hydrogen and sulfur atoms is shown in angstroms. (*E*) The distances and angles of the hydrogen bonds. The distance/angle between the hydrogen and the sulfur are shown on the left and the center columns, and the distance between nitrogen/oxygen and sulfur

643 are shown on the right column. (*F*) Hydrogen bond between Thr63-OH and the main chain –CO of
644 Thr10.
645
646 **Fig. 3 DFT calculation based on the neutron structure of [4Fe-4S] *Bt*Fd**
647 (*A*) Illustration of model structures (CM_N, CM, and CM_H) and their calculated *IP* values. (*B*) Assumed
648 charge/spin states of the [4Fe-4S] cluster for Ox and Red states. Fe1 is indicated by the orange
649 underscore and dominantly changes its charge state. (*C*) Distribution of LUMOs of CM and CM_H.
650 The red and green colors indicate positive and negative phases, respectively.
651
652 **Fig. 4 Spectral changes upon [4Fe-4S] cluster oxidation and typical voltammogram of *Bt*Fd and**
653 **its mutant proteins** (*A*) Time-dependent changing of UV-vis absorption spectrum of wild-type *Bt*Fd
654 by air oxidation. The spectra are colored in rainbow colors from red (reduced BtFd) to purple
655 (oxidated BtFd). The arrows indicate the absorbance increase at 340 nm, 420 nm, and indicate the
656 absorbance decrease at 260 nm. (*B*) The absorption changes of the Asp64 mutated BtFds at 420 nm
657 recorded every second. The standard deviations calculated from at least 3 times the measurements
658 indicated as the line width with the light color. The $T_{1/2}$ value (sec) is indicated in the inset. (*C*) The
659 cyclic voltammograms obtained at the disposable screen-printed carbon electrode from a solution of
660 as isolated 100 μM *Bt*Fd or its mutated proteins in 50 mM Tris-HCl (pH 7.0), 150 mM NaCl and 2.5
661 mM neomycin, at sweep rate of 50 mV/s. The CV measurement performed in the anerobic chamber
662 (O_2 < 5 ppm).
663

664 **Fig. 5 The effect of aspartate/glutamate residue in various ferredoxins harboring the low-**

665 **potential [4Fe-4S] cluster**

666 (*A*) Pyrogenetic tree of ferredoxin harboring the [4Fe-4S], [4Fe-4S] x 2 and [3Fe-4S] cluster from

667 various organism. (*B*) The air-oxidation absorption changes at 420 nm of various ferredoxin and its

668 Asp/Glu mutated ferredoxin are also indicated.

669

Fig. 1

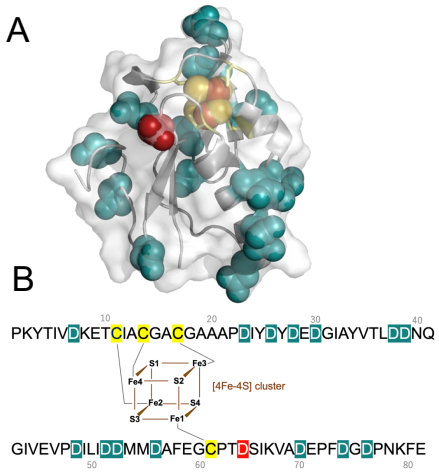

Ternary and primary structures of low-potential [4Fe-4S] *Bt*Fd.
(*A*) The 3D structure of BtFd (PDB id: 1IQZ). The [4Fe-4S] cluster and aspartate residues are shown as a space-filling model, and the ligand cysteines for the Fe-S cluster are shown as yellow sticks. The surface drawing is superposed on the cartoon model. (*B*) Whole amino acid sequence of BtFd. The ligating manner of the [4Fe-4S] cluster is illustrated, and the ligand cysteine and aspartate residues are highlighted.

Fig. 2

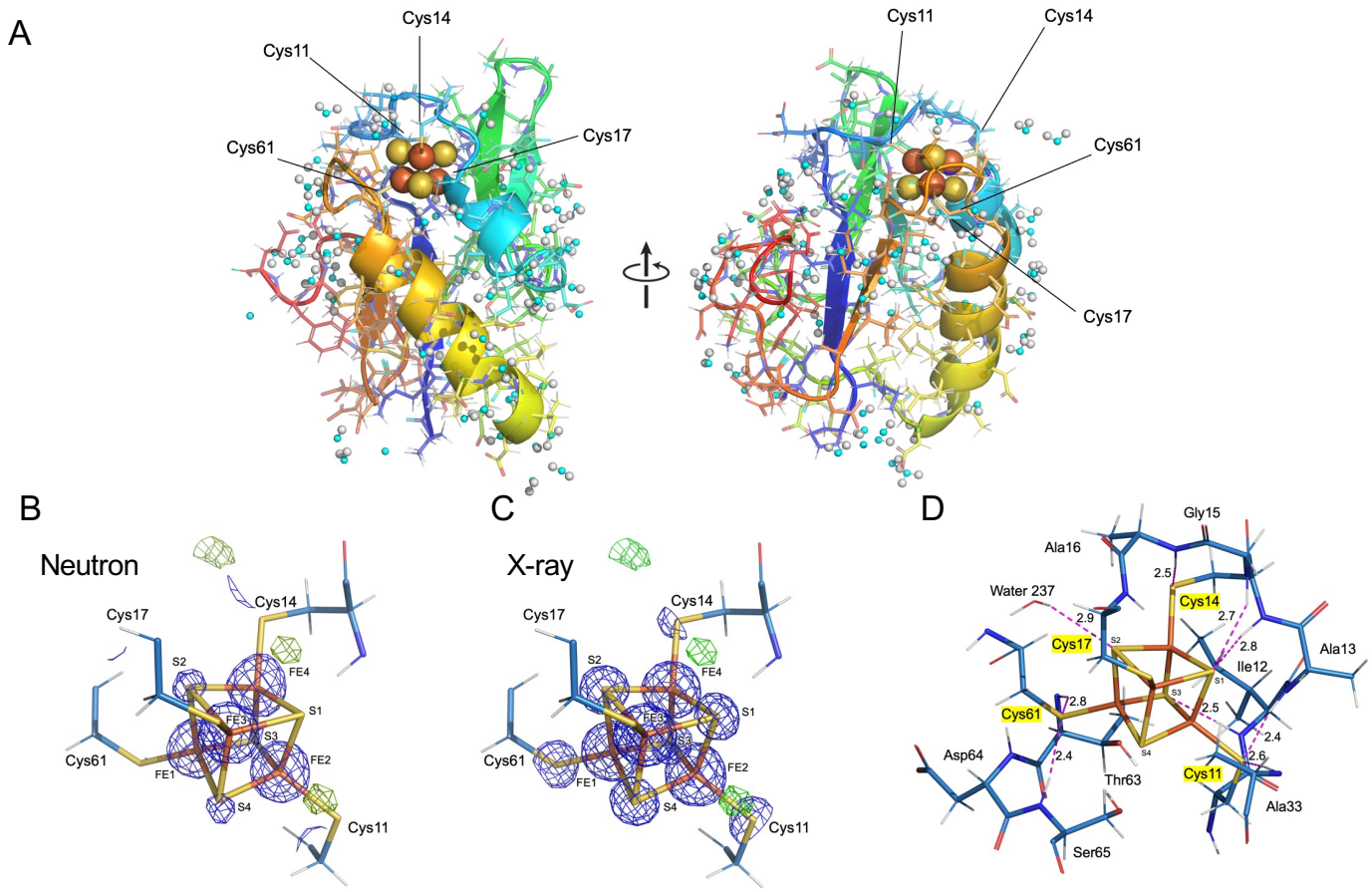

E

Atoms	H…S Distance (Å)	H…S Angle (˚)	N/O…S Distance (Å)
NH (I12).....S3(FeS)	2.5	159.8	3.5
NH (A13).....Sᵞ(C11)	2.4	166.3	3.4
NH (C14).....S1(FeS)	2.8	127.0	3.5
NH (G15).....S1(FeS)	2.7	151.5	3.5
NH (A16).....Sᵞ(C14)	2.5	164.3	3.5
NH (A33).....Sᵞ(C11)	2.6	166.3	3.6
NH (T63).....Sᵞ(C61)	2.8	149.6	3.7
NH (S65).....Sᵞ(C61)	2.4	159.9	3.3
OH (Water 237).....S2(FeS)	2.9	140.0	3.6

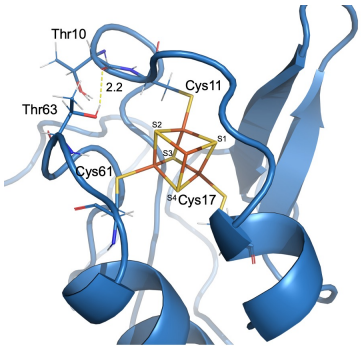

Neutron structure of low-potential [4Fe-4S] *Bt*Fd

(*A*) Overall neutron structure of *Bt*Fd. *Bt*Fd polypeptides are colored in rainbow colors from blue (N-terminus) to red (C-terminus). The [4Fe-4S] cluster and water molecules are shown as a space-filling model. White and cyan balls indicate hydrogen (deuterium) and oxygen atoms, respectively. The figure on the right is the left one rotated approximately 90˚ . (*B*) The $2F_o$–F_c (1.0 sigma: blue cage) and F_o–F_c (3.0 sigma: green cage) neutron-scattering length density map around the [4Fe-4S] cluster and the structural model. The $2F_o$–F_c map is shown within 1 Å around the [4Fe-4S] cluster for clarity. (*C*) X-ray electron density map of the corresponding region of (*B*). $2F_o$–F_c (5.0 sigma) and F_o–F_c (3.0 sigma) maps are shown in blue and green, respectively. (*D*) Hydrogen bond with the [4Fe-4S] cluster and its ligand Sγ atoms of cysteines. The hydrogen (deuterium), oxygen, carbon, and nitrogen atoms are shown in white, red, cyan, and blue, respectively. The hydrogen bonds indicate pink broken lines and the distance between the amide hydrogen and sulfur atoms is shown in angstroms. (*E*) The distances and angles of the hydrogen bonds. The distance/angle between the hydrogen and the sulfur are shown on the left and the center columns, and the distance between nitrogen/oxygen and sulfur are shown on the right column. (*F*) Hydrogen bond between Thr63-OH and the main chain –CO of Thr10.

Fig. 3

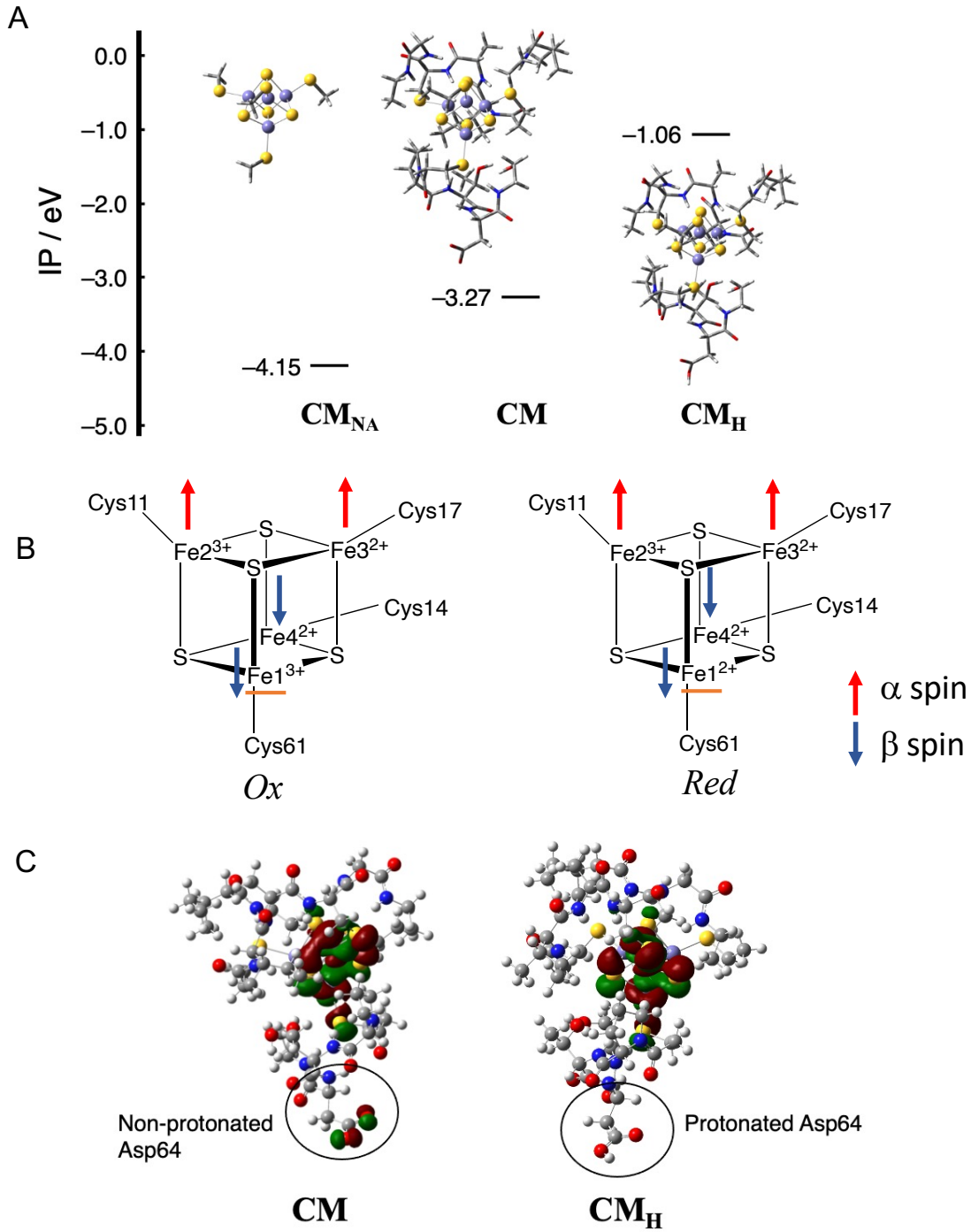

DFT calculation based on the neutron structure of [4Fe-4S] *Bt*Fd
(*A*) Illustration of model structures (CM_N, CM, and CM_H) and their calculated *IP* values. (*B*) Assumed charge/spin states of the [4Fe-4S] cluster for Ox and Red states. Fe1 is indicated by the orange underscore and dominantly changes its charge state. (*C*) Distribution of LUMOs of CM and CM_H. The red and green colors indicate positive and negative phases, respectively.

Fig. 4

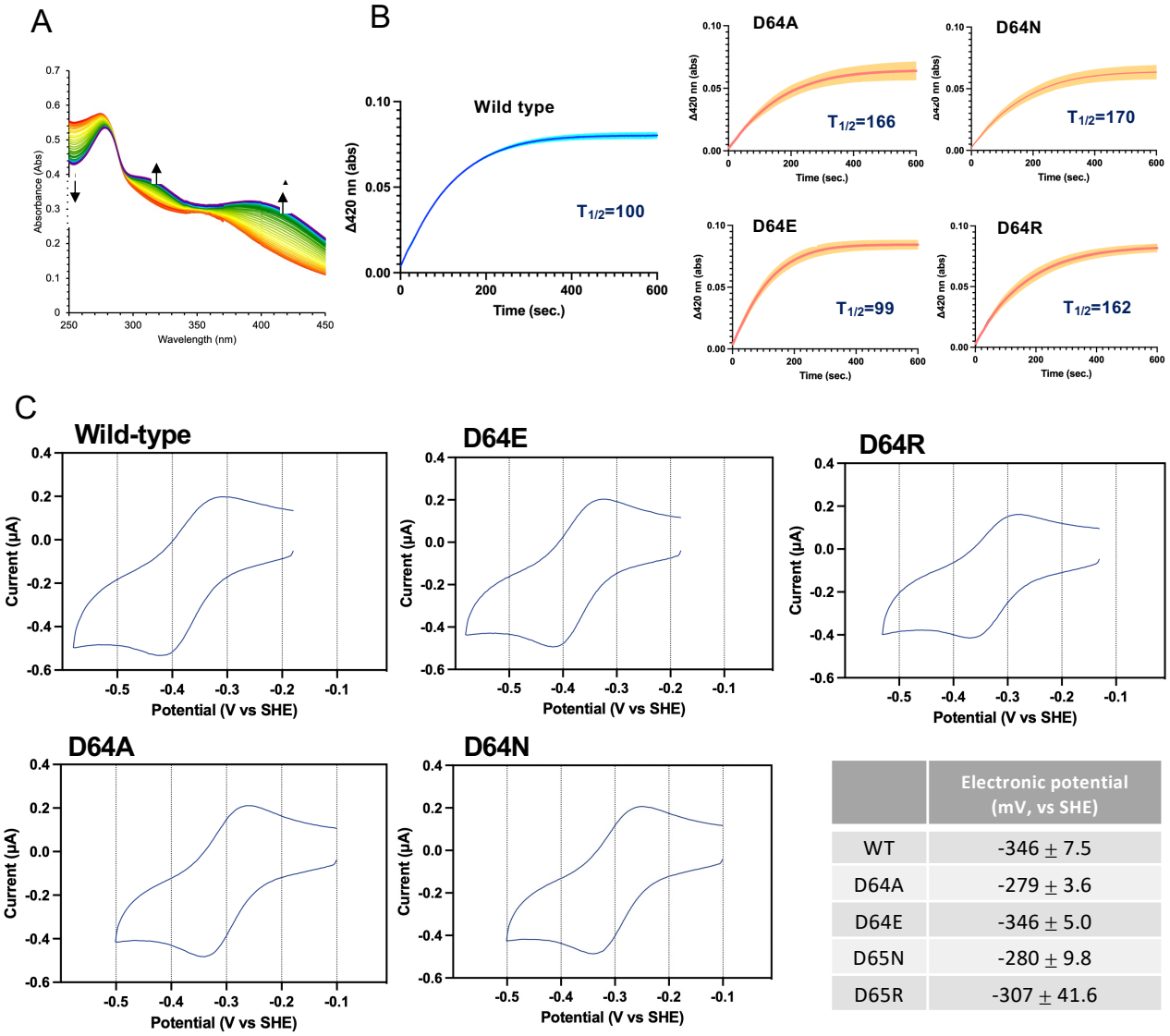

	Electronic potential (mV, vs SHE)
WT	-346 ± 7.5
D64A	-279 ± 3.6
D64E	-346 ± 5.0
D65N	-280 ± 9.8
D65R	-307 ± 41.6

Spectral changes upon [4Fe-4S] cluster oxidation and typical voltammogram of *Bt*Fd and its mutant proteins (*A*) Time-dependent changing of UV-vis absorption spectrum of wild-type *Bt*Fd by air oxidation. The spectra are colored in rainbow colors from red (reduced BtFd) to purple (oxidated BtFd). The arrows indicate the absorbance increase at 340 nm, 420 nm, and indicate the absorbance decrease at 260 nm. (*B*) The absorption changes of the Asp64 mutated BtFds at 420 nm recorded every second. The standard deviations calculated from at least 3 times the measurements indicated as the line width with the light color. The $T_{1/2}$ value (sec) is indicated in the inset. (*C*) The cyclic voltammograms obtained at the disposable screen-printed carbon electrode from a solution of as isolated 100 μM *Bt*Fd or its mutated proteins in 50 mM Tris-HCl (pH 7.0), 150 mM NaCl and 2.5 mM neomycin, at sweep rate of 50 mV/s. The CV measurement performed in the anerobic chamber (O_2 < 5 ppm).

Fig. 5

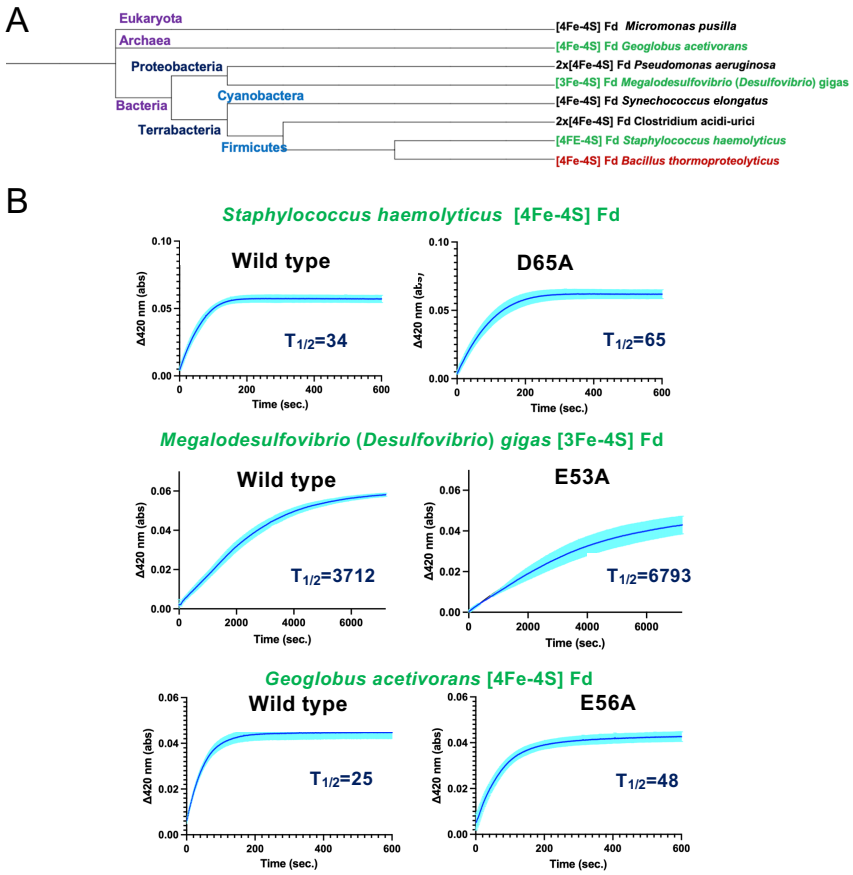

The effect of aspartate/glutamate residue in various ferredoxins harboring the low-potential [4Fe-4S] cluster (*A*) Pyrogenetic tree of ferredoxin harboring the [4Fe-4S], [4Fe-4S] x 2 and [3Fe-4S] cluster from various organism. (*B*) The air-oxidation absorption changes at 420 nm of various ferredoxin and its Asp/Glu mutated ferredoxin are also indicated.

Table 1. Statistics for Neutron and X-ray Diffraction Data

Data Collection		
	Neutron	X-ray
Beamline	iBIX at MLF in J-PARC	NW12A at PF-AR
Wavelength (Å)	1.5 – 4.5	1.0000
Exposure time	6 hours/1 set	0.5 second/0.5°
Number of datasets (neutron) or images (X-ray)	58 (15 days)	720
Transmittance (%)	100	5
Resolution (Å)	15.12 – 1.60 (1.69 – 1.60)	50.00 – 1.45 (1.48 – 1.45)
Space group	*C*2	
Cell parameters (Å, °)	*a* = 70.5, *b* = 37.9, *c* = 33.0 β = 106.0	
Multiplicity	7.5 (6.2)	6.7 (6.1)
Completeness (%)	94.2 (76.8)	100 (100)
R_{merge}	0.137 (0.369)	0.080 (0.553)
$I/\sigma(I)$	12.9 (4.9)	25.2 (2.5)
Joint refinement		
R_{work}/R_{free}	0.167/0.184	0.147/0.159
r.m.s Bond lengths (Å)	0.010	–
r.m.s Bond angles (°)	1.067	–
Total No. of hydrogen atom	598	–
Total No. of deuterium atom	221	–
No. of H atoms in protein	598	–
No. of D atoms in protein	110	–
No. of H atoms in water	0	–
No. of D atoms in water	111	–

Supporting Information for
Protonation/deprotonation-driven switch for the redox stability of low-potential [4Fe-4S] ferredoxin

Kei Wada, Kenji Kobayashi, Iori Era, Yusuke Isobe, Taigo Kamimura, Masaki Marukawa, Takayuki Nagae, Kazuki Honjo, Noriko Kaseda, Yumiko Motoyama, Kengo Inoue, Masakazu Sugishima, Katsuhiro Kusaka, Naomine Yano, Keiichi Fukuyama, Masaki Mishima, Yasutaka Kitagawa, Masaki Unno

Corresponding authors: Kei Wada, Yasutaka Kitagawa, Masaki Unno
Email: keiwada@med.miyazaki-u.ac.jp; kitagawa@cheng.es.osaka-u.ac.jp; masaki.unno.19@vc.ibaraki.ac.jp

This PDF file includes:

Supporting text
Figures S1 to S9
Tables S1 to S5
SI References

Supplementary Text

pKa estimation of Asp64 in BtFd by NMR spectroscopy

The stable isotopically labeled BtFd proteins were expressed in a 2 L M9 minimal medium containing 0.5 g/L $^{15}NH_4Cl$, with 4 g/L of unlabeled glucose, 1 g/L of $^{13}C_6$-glucose for ^{15}N, or $^{13}C/^{15}N$ labeled as sole nitrogen and carbon sources, respectively. After induction, the cultures were incubated overnight at 25 °C, and the cells were harvested by centrifugation. The purification was performed in the same manner to the crystallization. The NMR sample for standard heteronuclear experiments was dissolved in 50 mM K-phosphate buffer (pH 6.9) containing 50 mM KCl and 7% D_2O. The final concentrations of BtFd in the samples were 0.9–1.5 mM in a final volume of 300 mL. Microcell NMR tubes (Shigemi) were used. All NMR spectra were processed with the software package NMRPipe (*1*) and analyzed using Sparky (*2*). All NMR experiments were performed at 303 K on a Bruker AVANCEIII(HD)600 instrument equipped with a TCI CRYOPROBE. As a first step for analyzing the p*K*a of the aspartate sidechains, we established the resonance assignments by standard heteronuclear multidimensional NMR technique (*3*). The backbone resonance assignments were obtained from the following two- and three-dimensional experiments: 2D ^1H-^{15}N HSQC, 3D HNCO, HN(CA)CO, CBCA(CO)NH, and HNCACB. The sidechain aliphatic ^1H and ^{13}C assignments were obtained from the following three- and four-dimensional experiments: 3D C(CO)NH, 3D H(CCO)NH, 3D HCCH-TOCSY, and 4D HC(CO)NH (*4*). Based on the obtained aliphatic assignments, the ^{13}CO(g) resonance assignments of the aspartate sidechains were made by linking the adjacent ^{13}Cb chemical shifts. Since the CO signals in the 1D ^{13}C experiment were heavily overlapped, we used the 2D CACO experiment (*5*) in which the ^{13}Ca offset of indirect dimension was shifted to $^{13}C\beta$ (45 ppm) for monitoring the titrated signals. Namely, we diverted a CACO experiment originally used for correlations of backbone $C\alpha$ and CO to the sidechain CO assignment. To avoid the signal splitting caused by ^{13}C-^{13}C spin coupling during ^{13}CO acquisition, low-bash homonuclear decoupling (*6*) was achieved in the experiments. The pH 3.5 buffer was composed of 50 mM phosphate and 50 mM KCl, the pH 4.0–5.0 buffer was composed of 50 mM acetate and 50 mM KCl, the pH 5.5–6.5 buffer was composed of 50 mM MES and 50 mM KCl, the pH 7.0–8.0 buffer was composed of 50 mM HEPES and 50 mM KCl, and the pH 8.5–9.0 buffer was composed of CHES and 50 mM KCl. These buffers contained 7% D_2O for the lock signal. The p*K*a(s) were estimated from the Hill equation by nonlinear least-square curve fitting using Microsoft Excel implemented SOLVER module (Microsoft).

BtFd was stable enough to conduct the NMR experiments under acidic to basic conditions (pH 3.5–9.0), thus, we were able to estimate the p*K*a of aspartate sidechains by monitoring the chemical shifts of $^{13}CO(\gamma)$ (Fig. S7A). Notably, $^{13}CO(\gamma)$ resonance of Asp64 is isolated from the others, and showed remarkable chemical shift changes upon pH titration (Fig. S7, A and B). The sigmoidal curve was obtained from the Asp64 signals and the p*K*a was estimated to be 4.9 (Fig. S7B). The p*K*a value of Asp74 was also able to be estimated to be 5.0, although its chemical shift change was smaller than that of Asp64. The p*K*a values of the other residues were not able to be evaluated, since they showed no sigmoidal curves in the pH range of 3.5–9.0, or their signals were not reliably assigned. Interestingly, the p*K*a value of Asp74 was also shifted to a natural pH (Fig. S7B). This Asp74 is located away from the [4Fe-4S] cluster at a distance of 22.4 Å (Table S5), and the distance between Asp64 and Asp74 is approximately 10.1 Å. The function of Asp74 is unclear at this stage.

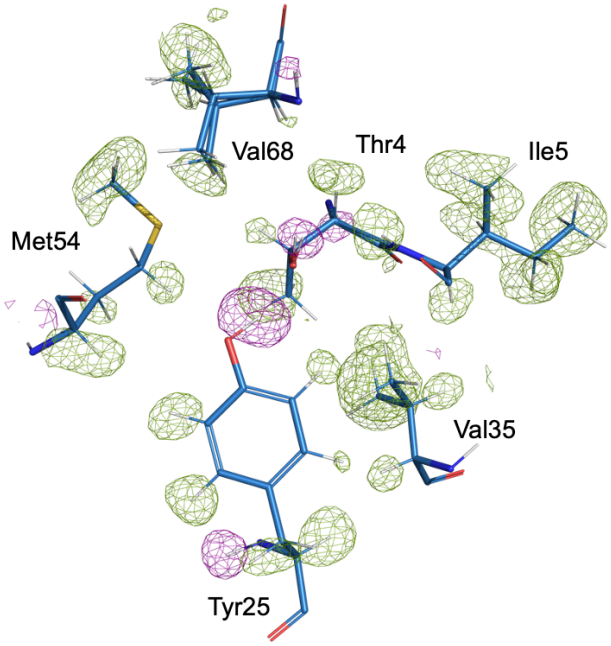

Fig. S1. Neutron-scattering length density maps of [4Fe-4S] ferredoxins.
The F_o–F_c neutron-scattering length density omits maps for the hydrogen/deuterium at 2.0 σ contour levels. The pink and green cages represent the +(F_o–F_c) and –(F_o–F_c) map, respectively, and the final model of *Bt*Fd is superposed on the maps. The maps clearly indicate that the densities derived from the deuterium and hydrogen atoms are clearly visible in the neutron crystallography.

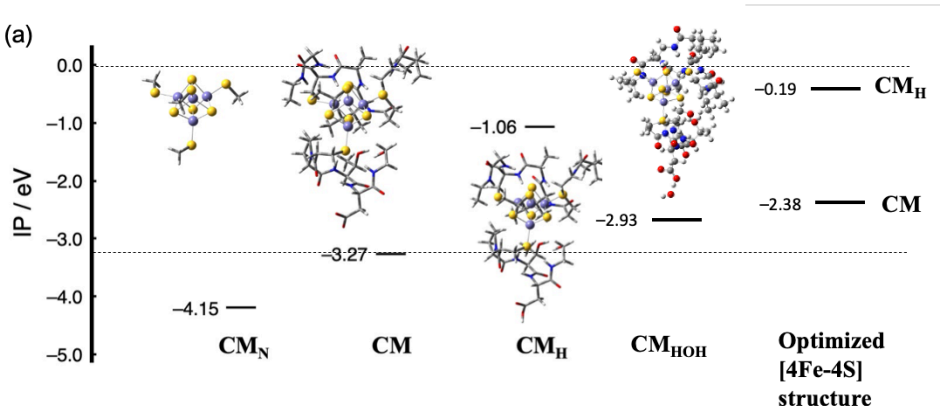

Fig. S2. DFT calculation based on the neutron structure of [4Fe-4S] BtFd Calculated IP values of each model.

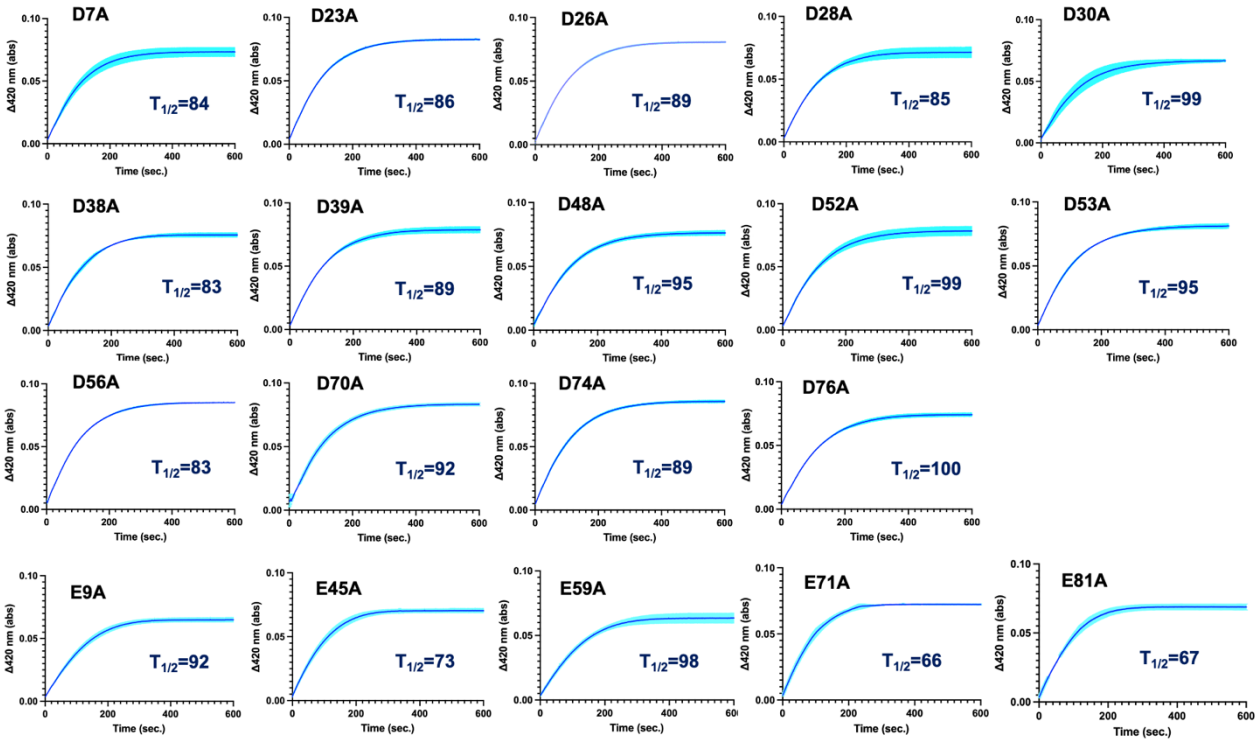

Fig. S3. The absorption changes of various mutated *Bt*Fds at 420 nm recorded every second. The standard deviations calculated from at least 3 times the measurements indicated as the line width with the light color. The $T_{1/2}$ value (sec) is indicated in the inset.

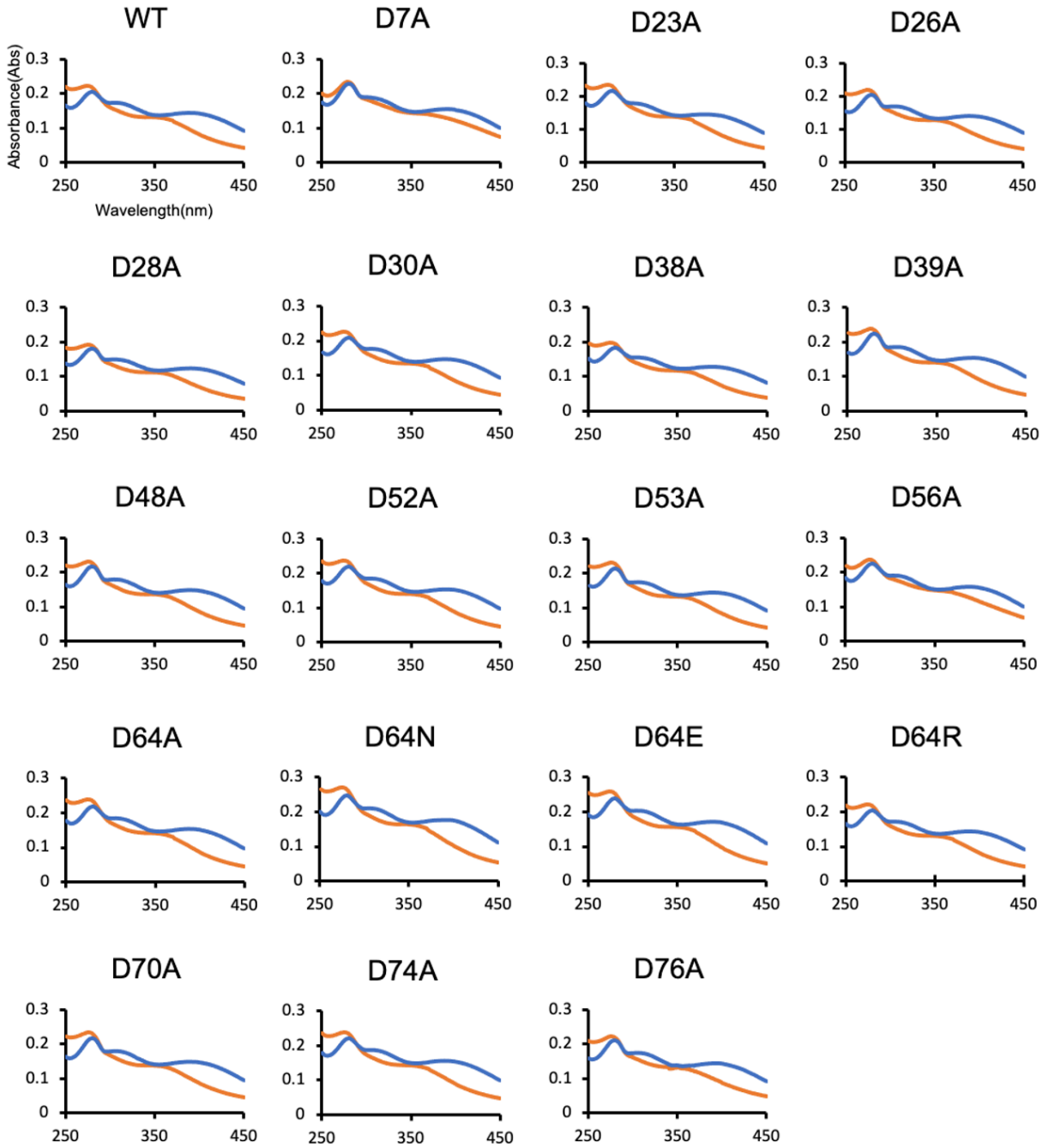

Fig. S4. UV-Vis absorption spectroscopy of *Bt*Fd and its mutant proteins.
The spectra of reduced *Bt*Fds are indicated by the orange line and those of completely air-oxidated *Bt*Fds are indicated by the blue line. Wild-type *Bt*Fd and its mutated proteins showed very similar spectra.

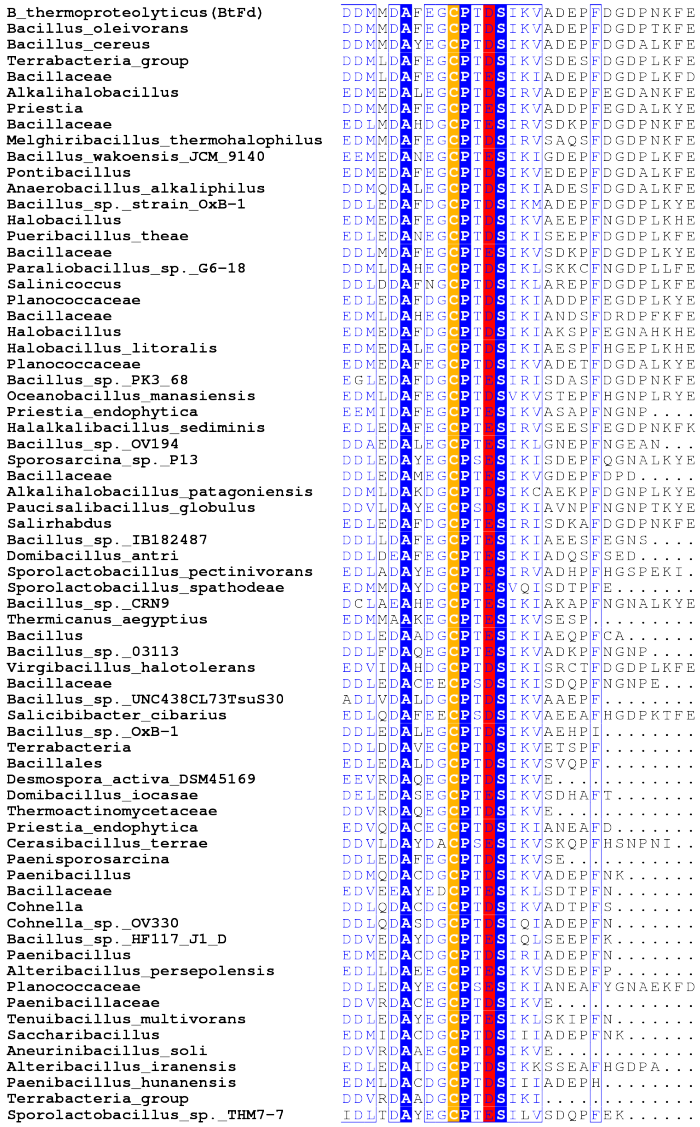

Fig. S5. Conserved amino acid residues of [4Fe-4S] ferredoxins from several species. Cysteine residues for the ligand for the Fe-S cluster are completely conserved (orange-highlighted) and several residues around the cysteines are also highly conserved (blue-highlighted). The corresponding residues of Asp64 in BtFd are conserved in negatively charged residues (Asp or Glu: red-highlighted). This figure is prepared using ESpript ver3.0 server (https://espript.ibcp.fr/ESPript/ESPript/index.php).

```
                                                                                  1        10        20        30
[4Fe-4S]Fd_Bacillus                 ....................................PKYTIVDKETCIACGACGAAAPDIYDYDEDGIAYV
[4Fe-4S]Fd_Micromonas_pusilla       ............................LGPDSETKAIFVDESTCIGCRACVTWAAGTFEMVEDQNA..
[4Fe-4S]Fd_Geoglobus_acetivora      ....................................MMKVVIDESTCTGCGTCESICPEVFQLGDDG....
2[4e-4S]Fd_Pseudomonas_aerugi       ......................................SLKITDDCINCDVCEPECPNGAISQGEEI...
[3Fe-4S]Fd_Desulfovibrio_gigas      ......................................PIEVNDDCMACEACVEICPDVFEMNEEG....
[4Fe-4S]Fd_Synechococcus_elong      MTTPDRSGLEPELGGSLRHGQARSGLEPELGGELRQKLVWVDEVTCIGCRYCSHVATNTFYIEPDY....
2[4Fe-4S]Fd_Clostridium_acidi-      ......................................AYVINEACISCGACEPECPVNAISSGDDR...
[4Fe-4S]Fd_Staphylococcus_haem      ....................................MAKYTIVDMDTCIACGACGAAAPDIYDYDDEGIAFV

                                        40        50        60        70        80
[4Fe-4S]Fd_Bacillus                 TLDDNQGIVEVPDILIDDMMDAFEGCPTDSIKVADEPFDGDPNKFE.....................
[4Fe-4S]Fd_Micromonas_pusilla       ...GRARCTRQWNDDEETMQIAVEMCPVDCIYWVKRSQLAILE........................
[4Fe-4S]Fd_Geoglobus_acetivora      ....LAHVVGECEGLEECCQEAADNCPVEAITIE.................................
2[4e-4S]Fd_Pseudomonas_aerugi       ..YVIDPNLCTECVGHYDEPQCQQVCPVDCIPLDDANVESKDQLMEKYRKITG..............
[3Fe-4S]Fd_Desulfovibrio_gigas      ....DKAVVINPDSDLDCVEEAIDSCPAEAIVRS.................................
[4Fe-4S]Fd_Synechococcus_elong      ...GRSRVVRQNGDPEELVQEAIDTCPVDCIHWVNPSELRQLEAERRNQVIMPLGFPQERSKQRRRT
2[4Fe-4S]Fd_Clostridium_acidi-      ..YVIDADTCIDCG......ACAGVCPVDAPVQA.................................
[4Fe-4S]Fd_Staphylococcus_haem      ILDDNQGTAEVPEELYEDMEDALEGCPTDSIKIEEEPFDGDALKFE.....................
```

Fig. S6. Sequence alignment of [4Fe-4S], [4Fe-4S]x2 and [3Fe-4S] ferredoxins from various organisms.

Cysteine residues for the ligand for the Fe-S cluster are completely conserved (yellow-highlighted) and several residues around the cysteines are also highly conserved (blue-highlighted). The corresponding residues of Asp64 in BtFd are conserved in negatively charged residues (Asp or Glu: pink font). This figure is prepared using the Consurf server (https://consurf.tau.ac.il/index_proteins.php) and ESpript ver3.0 server (https://espript.ibcp.fr/ESPript/ESPript/index.php).

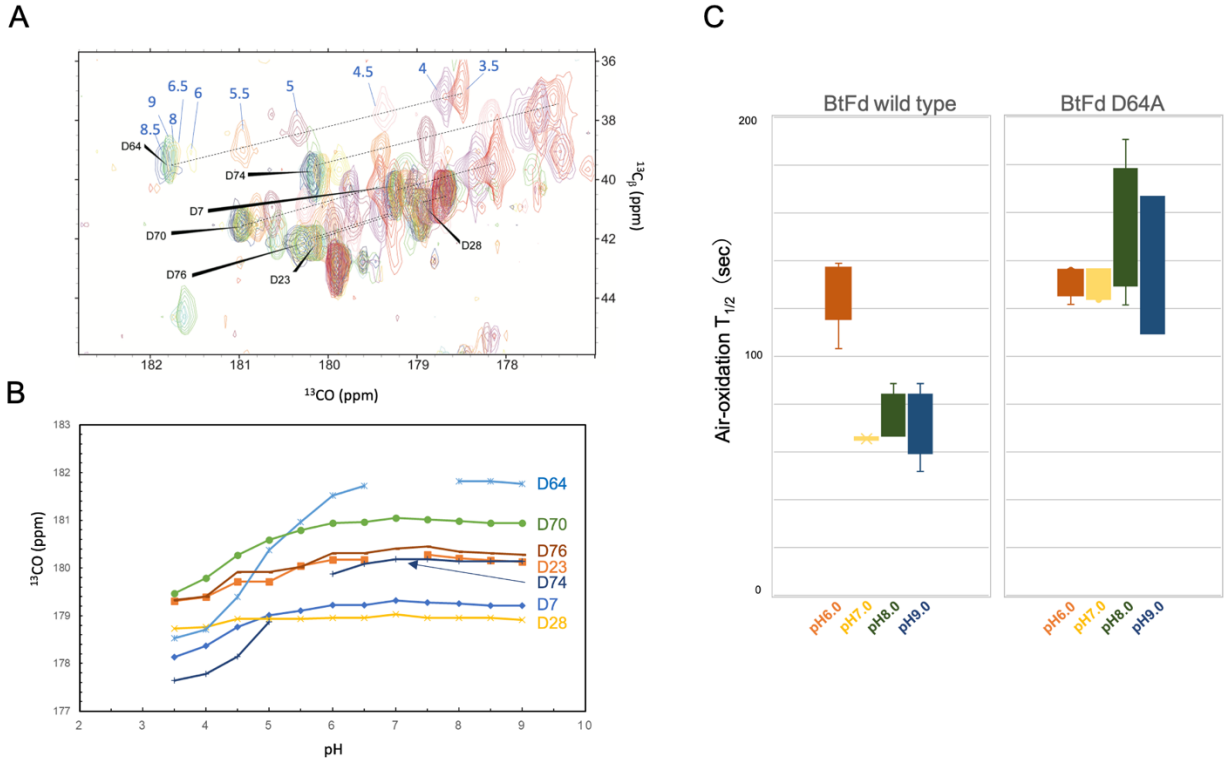

Fig. S7. The p*K*a estimation of the Asp64 in *Bt*Fd (A) A close-up view of an overlay of the of the CACO experiments (Cβ offset) of NMR. The assignments were indicated. For Asp64 signals, corresponding pH values are shown in blue as a representative of titrations. Chemical shift changes are indicated by black dotted line for each residue. Detail information were described in the supplemental method and text. (B)Titration curves obtained from the CACO experiments (Cβ offset). The points correspond to pH 7.0 and 7.5 are missing in a series of Asp64, and the point corresponds to pH 6.5 is missing in a series of Asp74. (C) The oxidation rates of *Bt*Fd wild-type and D64A under the different pH conditions.

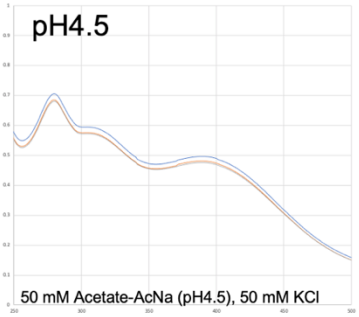

	0h	15h	25h
304nm/280nm	0.842	0.841	0.840
388nm/280nm	0.702	0.702	0.699
304nm/388nm	1.199	1.198	1.202

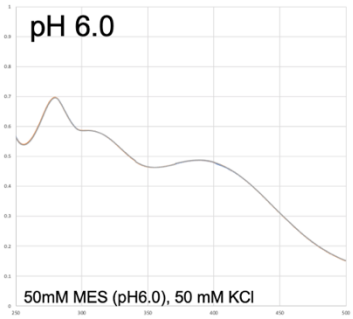

	0h	15h	25h
304nm/280nm	0.842	0.842	0.842
388nm/280nm	0.700	0.700	0.701
304nm/388nm	1.204	1.203	1.201

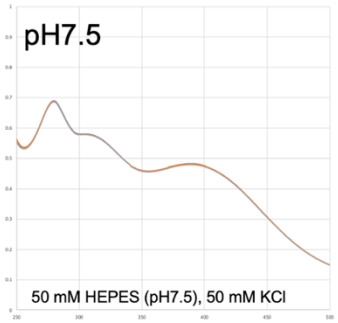

	0h	15h	25h
304nm/280nm	0.842	0.842	0.842
388nm/280nm	0.700	0.702	0.698
304nm/388nm	1.201	1.200	1.206

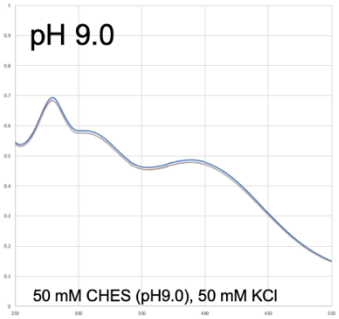

	0h	15h	25h
304nm/280nm	0.842	0.842	0.842
388nm/280nm	0.702	0.700	0.700
304nm/388nm	1.200	1.202	1.203

Fig. S8. Stability of [4Fe-4S] cluster in *Bt*Fd under the different pH conditions. The UV-Vis absorbance ratios of 304 nm/280 nm, 388 nm/280 nm and 304 nm/388 nm are shown in the table below each spectral panel.

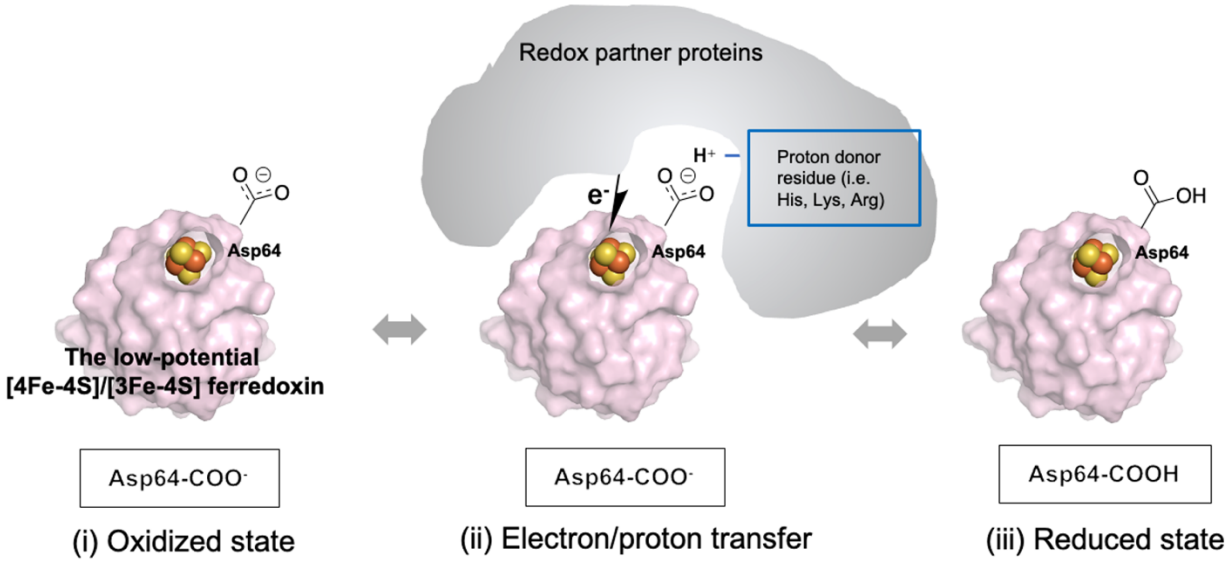

Fig. S9. Proposed putative mechanism of the low-potential ferredoxin.
(i) The deprotonation state of the aspartate residue (Asp-COO$^-$) neighboring the oxidated [4Fe-4S]/[3Fe-4S] cluster is the receivable state of an electron. (ii) When the electron-donor protein forms a complex with ferredoxin, the electrons move to the [4Fe-4S]/[3Fe-4S] cluster instantaneously. (iii) Next, the aspartate residue accepts the proton for neutralization (Asp-COOH), and the reduced state of [4Fe-4S]/[3Fe-4S] clusters is stabilized.

Table S1. Cartesian coordinate of CM_H used for the DFT calculations

atom	*x* / Å	*y* / Å	*z* / Å	*x* / Å	*y* / Å	*z* / Å	*x* / Å
Fe	51.156	26.907	-3.179	C	54.743	28.460	-1.565
Fe	48.980	28.449	-3.585	H	56.554	27.390	0.793
Fe	50.443	27.558	-5.708	H	55.043	29.582	1.547
Fe	51.472	29.467	-3.999	H	56.424	29.637	0.416
S	49.681	29.696	-5.349	H	53.459	29.555	-0.186
S	52.523	27.621	-4.827	H	54.736	30.548	-0.942
S	50.558	28.775	-2.049	H	55.562	28.730	-2.232
S	49.293	26.313	-4.232	N	53.408	26.740	1.466
N	48.058	30.492	-0.277	C	52.479	26.302	2.502
C	48.219	31.919	-0.009	C	52.033	24.858	2.334
C	48.373	32.739	-1.294	O	51.037	24.440	2.919
O	48.790	33.898	-1.240	C	51.274	27.224	2.544
C	49.362	32.179	0.994	O	50.717	27.319	1.226
C	50.663	31.594	0.458	C	51.683	28.622	3.012
C	49.044	31.580	2.341	H	52.994	26.365	3.461
C	51.905	32.039	1.231	H	50.532	26.832	3.239
H	47.297	32.268	0.456	H	50.801	29.255	3.109
H	49.470	33.257	1.113	H	52.182	28.559	3.980
H	50.608	30.506	0.515	H	52.365	29.072	2.291
H	50.788	31.907	-0.579	H	52.996	26.764	0.533
H	49.851	31.818	3.035	H	49.739	27.288	1.273
H	48.106	32.000	2.704	N	52.739	24.097	1.524
H	48.952	30.499	2.237	C	52.447	22.665	1.388
H	51.935	31.514	2.186	C	50.999	22.421	0.957
H	52.792	31.797	0.647	O	50.377	21.434	1.348
H	51.851	33.114	1.399	C	52.807	21.865	2.656
H	48.919	30.035	-0.577	C	54.316	21.837	2.927
N	48.006	32.177	-2.459	O	55.107	21.756	1.965
C	47.922	32.940	-3.709	H	53.083	22.274	0.594
C	49.249	33.579	-4.101	H	52.318	22.322	3.516
O	49.289	34.735	-4.534	H	52.466	20.836	2.537
C	46.811	33.991	-3.658	H	53.515	24.428	0.950
H	47.015	34.684	-2.842	N	50.463	23.310	0.125
H	46.787	34.530	-4.605	C	48.604	24.612	-0.759
H	45.856	33.492	-3.491	O	48.641	25.501	0.378
H	47.761	31.192	-2.562	H	49.257	24.999	-1.542
N	50.339	32.821	-3.970	H	47.581	24.541	-1.129
C	51.682	33.345	-4.188	H	50.971	24.109	-0.253
C	52.133	33.338	-5.642	H	49.569	25.652	0.655
O	53.113	34.018	-5.958	H	53.842	28.258	-2.144
C	52.691	32.574	-3.340	C	54.867	25.648	-2.573

S	53.161	30.980	-3.986	H	55.881	25.386	-2.790
H	51.680	34.387	-3.867	H	54.491	26.286	-3.345
H	53.599	33.172	-3.255	C	49.084	23.239	-0.339
H	52.258	32.412	-2.353	H	48.350	22.946	0.382
H	50.323	31.834	-3.713	H	49.166	22.483	-1.092
N	51.471	32.597	-6.531	O	54.717	21.901	4.118
C	51.828	32.597	-7.941	H	55.079	21.052	4.381
C	52.971	31.678	-8.370	C	44.136	29.698	-6.554
O	53.291	31.646	-9.569	O	43.373	29.594	-7.527
H	50.948	32.303	-8.513	C	42.720	30.361	-4.590
H	52.110	33.612	-8.220	C	42.430	31.428	-3.521
H	50.685	31.990	-6.300	C	42.981	29.008	-3.942
N	53.583	30.912	-7.458	C	43.569	31.718	-2.601
C	55.472	29.647	-6.552	H	41.838	30.289	-5.226
H	55.963	30.501	-6.085	H	42.169	32.359	-4.023
H	54.745	29.214	-5.865	H	41.594	31.087	-2.910
H	56.214	28.897	-6.829	H	43.199	28.278	-4.721
H	53.297	30.825	-6.483	H	43.831	29.097	-3.266
C	46.889	29.856	-0.139	H	42.094	28.705	-3.386
H	47.678	32.225	-4.495	H	43.174	31.997	-1.624
S	46.811	29.076	-3.190	H	44.189	30.826	-2.510
C	46.231	28.098	-1.820	H	44.157	32.539	-3.012
H	45.445	28.621	-1.316	N	45.177	28.897	-6.365
H	45.862	27.161	-2.182	C	46.957	27.364	-7.072
O	45.859	30.407	0.236	H	47.143	26.500	-7.710
C	46.900	28.370	-0.456	H	47.689	28.145	-7.280
H	46.342	27.619	0.062	H	47.015	27.070	-6.024
H	47.940	28.260	-0.231	H	45.775	28.909	-5.539
C	54.749	30.117	-7.808	C	45.558	27.903	-7.361
H	55.572	30.565	-8.324	H	45.577	28.326	-8.344
H	54.248	29.433	-8.461	H	44.800	27.150	-7.311
C	55.189	26.023	-1.124	C	43.907	30.756	-5.480
O	55.475	25.135	-0.325	H	44.808	30.834	-4.908
C	53.647	24.744	-2.630	H	43.682	31.704	-5.922
S	52.213	25.438	-1.764	C	51.979	26.168	-8.183
H	53.369	24.590	-3.673	S	50.437	27.038	-7.918
H	53.892	23.789	-2.165	H	51.743	25.253	-8.726
N	55.102	27.304	-0.742	H	52.385	25.925	-7.201
C	55.518	27.685	0.626	C	53.058	26.931	-8.974
C	54.676	27.075	1.726	H	52.720	27.928	-9.167
O	55.181	26.899	2.841	H	53.962	26.965	-8.403
C	55.433	29.219	0.596	H	53.241	26.430	-9.902
C	54.492	29.567	-0.536				

Table S2. Examined charge/spin states with CM_{NA} model for (A) oxidized and (B) reduced states. Definition of Fe1–Fe4 is illustrated using CM below. o12 and r5 (indicated by yellow highlighted) were most stable states for *Ox* and *Red* states, respectively.

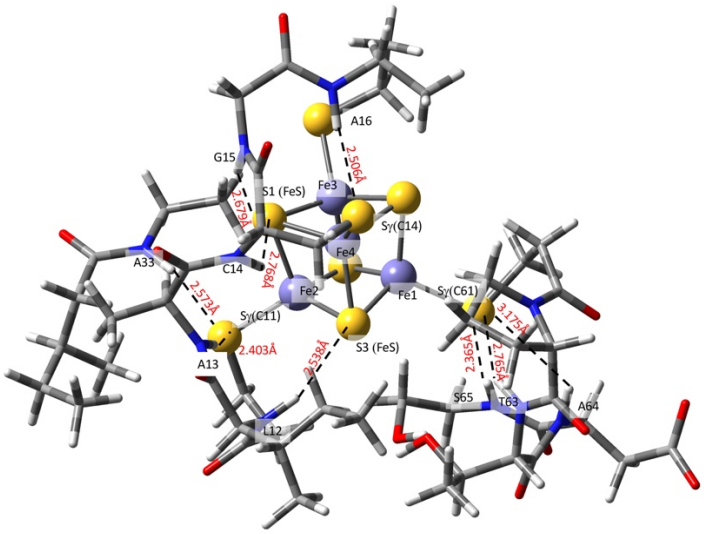

(A) Oxidized (*Ox*) state (u and d represent up and down spins)

Examined states	Fe1	Fe2	Fe3	Fe4	Energy / Hartree
charge	**2**	**2**	**3**	**3**	
o1	u	d	u	d	-8400.022791
o2	u	d	d	u	-8400.025020
charge	**2**	**3**	**2**	**3**	
o3	u	u	d	d	-8399.983854
o4	u	d	d	u	-8400.025019
charge	**2**	**3**	**3**	**2**	
o5	u	u	d	d	-8400.022702
o6	u	d	u	d	-8400.022789
charge	**3**	**2**	**3**	**2**	
o7	u	u	d	d	-8400.022689
o8	d	u	u	d	-8400.025019
charge	**3**	**2**	**2**	**3**	
o9	u	u	d	d	-8400.022693
o10	d	u	d	u	-8400.022801
charge	**3**	**3**	**2**	**2**	
o11	u	d	u	d	-8400.022802
o12	d	u	u	d	-8400.025022

(B) Reduced (*Red*) state (u and d represent up and down spins)

Examined states	Fe1	Fe2	Fe3	Fe4	Energy / Hartree
charge	3	2	2	2	
r1	u	u	d	d	-8399.871923
r2	u	d	u	d	-8399.870871
r3	u	d	d	u	-8399.871694
charge	2	3	2	2	
r4	u	u	d	d	-8399.871876
r5	d	u	u	d	-8399.872594
r6	d	u	d	u	-8399.869132
charge	2	2	3	2	
r7	u	d	u	d	-8399.870871
r8	d	u	u	d	-8399.872589
r9	d	d	u	u	-8399.867054
charge	2	2	2	3	
r10	u	d	d	u	-8399.871693
r11	d	u	d	u	-8399.869131
r12	d	d	u	u	-8399.656590

Table S3. Cartesian coordinate (in Å) of before and after the geometry optimization. (The Cartesian coordinate before the geometry optimization is the neutron structure)

Part 1. **CM** model

Before optimization				After optimization			
Fe	51.1560	26.9070	-3.1790	Fe	51.0899	26.8241	-3.0748
Fe	48.9800	28.4490	-3.5850	Fe	48.9077	28.4118	-3.6890
Fe	50.4430	27.5580	-5.7080	Fe	50.4026	27.5837	-5.8198
Fe	51.4720	29.4670	-3.9990	Fe	51.5173	29.5281	-4.0769
S	49.6810	29.6960	-5.3490	S	49.6463	29.7914	-5.5251
S	52.5230	27.6210	-4.8270	S	52.5245	27.5200	-4.9853
S	50.5580	28.7750	-2.0490	S	50.4549	28.9082	-2.0530
S	49.2930	26.3130	-4.2320	S	49.2273	26.1675	-4.3358
N	48.0580	30.4920	-0.2770	N	48.0580	30.4920	-0.2770
C	48.2190	31.9190	-0.0090	C	48.2190	31.9190	-0.0090
C	48.3730	32.7390	-1.2940	C	48.3730	32.7390	-1.2940
O	48.7900	33.8980	-1.2400	O	48.7900	33.8980	-1.2400
C	49.3620	32.1790	0.9940	C	49.3620	32.1790	0.9940
C	50.6630	31.5940	0.4580	C	50.6630	31.5940	0.4580
C	49.0440	31.5800	2.3410	C	49.0440	31.5800	2.3410
C	51.9050	32.0390	1.2310	C	51.9050	32.0390	1.2310
H	47.2970	32.2680	0.4560	H	47.2970	32.2680	0.4560
H	49.4700	33.2570	1.1130	H	49.4700	33.2570	1.1130
H	50.6080	30.5060	0.5150	H	50.6080	30.5060	0.5150
H	50.7880	31.9070	-0.5790	H	50.7880	31.9070	-0.5790
H	49.8510	31.8180	3.0350	H	49.8510	31.8180	3.0350
H	48.1060	32.0000	2.7040	H	48.1060	32.0000	2.7040
H	48.9520	30.4990	2.2370	H	48.9520	30.4990	2.2370
H	51.9350	31.5140	2.1860	H	51.9350	31.5140	2.1860
H	52.7920	31.7970	0.6470	H	52.7920	31.7970	0.6470
H	51.8510	33.1140	1.3990	H	51.8510	33.1140	1.3990
H	48.9190	30.0350	-0.5770	H	48.9190	30.0350	-0.5770
N	48.0060	32.1770	-2.4590	N	48.0060	32.1770	-2.4590
C	47.9220	32.9400	-3.7090	C	47.9220	32.9400	-3.7090

C	49.2490	33.5790	-4.1010	C	49.2490	33.5790	-4.1010
O	49.2890	34.7350	-4.5340	O	49.2890	34.7350	-4.5340
C	46.8110	33.9910	-3.6580	C	46.8110	33.9910	-3.6580
H	47.0150	34.6840	-2.8420	H	47.0150	34.6840	-2.8420
H	46.7870	34.5300	-4.6050	H	46.7870	34.5300	-4.6050
H	45.8560	33.4920	-3.4910	H	45.8560	33.4920	-3.4910
H	47.7610	31.1920	-2.5620	H	47.7610	31.1920	-2.5620
N	50.3390	32.8210	-3.9700	N	50.3390	32.8210	-3.9700
C	51.6820	33.3450	-4.1880	C	51.6821	33.3451	-4.1880
C	52.1330	33.3380	-5.6420	C	52.1330	33.3380	-5.6420
O	53.1130	34.0180	-5.9580	O	53.1130	34.0180	-5.9580
C	52.6910	32.5740	-3.3400	C	52.6908	32.5738	-3.3400
S	53.1610	30.9800	-3.9860	S	53.2923	30.9518	-3.9777
H	51.6800	34.3870	-3.8670	H	51.6800	34.3870	-3.8670
H	53.5990	33.1720	-3.2550	H	53.5990	33.1720	-3.2550
H	52.2580	32.4120	-2.3530	H	52.2581	32.4121	-2.3530
H	50.3230	31.8340	-3.7130	H	50.3230	31.8340	-3.7130
N	51.4710	32.5970	-6.5310	N	51.4710	32.5970	-6.5310
C	51.8280	32.5970	-7.9410	C	51.8280	32.5970	-7.9410
C	52.9710	31.6780	-8.3700	C	52.9710	31.6780	-8.3700
O	53.2910	31.6460	-9.5690	O	53.2910	31.6460	-9.5690
H	50.9480	32.3030	-8.5130	H	50.9480	32.3030	-8.5130
H	52.1100	33.6120	-8.2200	H	52.1100	33.6120	-8.2200
H	50.6850	31.9900	-6.3000	H	50.6850	31.9900	-6.3000
N	53.5830	30.9120	-7.4580	N	53.5830	30.9120	-7.4580
C	55.4720	29.6470	-6.5520	C	55.4720	29.6470	-6.5520
H	55.9630	30.5010	-6.0850	H	55.9630	30.5010	-6.0850
H	54.7450	29.2140	-5.8650	H	54.7450	29.2140	-5.8650
H	56.2140	28.8970	-6.8290	H	56.2140	28.8970	-6.8290
H	53.2970	30.8250	-6.4830	H	53.2970	30.8250	-6.4830
C	46.8895	29.8555	-0.1395	C	46.8895	29.8555	-0.1395
H	47.6780	32.2250	-4.4950	H	47.6780	32.2250	-4.4950

S	46.8110	29.0760	-3.1900	S	46.7360	29.1131	-3.2770
C	46.2315	28.0983	-1.8201	C	46.2318	28.0982	-1.8202
H	45.4454	28.6209	-1.3162	H	45.4454	28.6209	-1.3162
H	45.8624	27.1613	-2.1815	H	45.8623	27.1613	-2.1815
O	45.8590	30.4070	0.2360	O	45.8590	30.4070	0.2360
C	46.9000	28.3700	-0.4560	C	46.8999	28.3701	-0.4560
H	46.3416	27.6187	0.0623	H	46.3415	27.6187	0.0623
H	47.9403	28.2600	-0.2310	H	47.9403	28.2599	-0.2310
C	54.7490	30.1170	-7.8080	C	54.7490	30.1170	-7.8080
H	55.5724	30.5645	-8.3243	H	55.5724	30.5645	-8.3243
H	54.2480	29.4329	-8.4607	H	54.2480	29.4329	-8.4607
C	55.1890	26.0230	-1.1240	C	55.1890	26.0230	-1.1240
O	55.4750	25.1350	-0.3250	O	55.4750	25.1350	-0.3250
C	53.6470	24.7440	-2.6300	C	53.6470	24.7441	-2.6301
S	52.2130	25.4380	-1.7640	S	52.2470	25.4672	-1.6975
H	53.3690	24.5900	-3.6730	H	53.3690	24.5900	-3.6730
H	53.8920	23.7890	-2.1650	H	53.8920	23.7890	-2.1650
N	55.1020	27.3040	-0.7420	N	55.1020	27.3040	-0.7420
C	55.5180	27.6850	0.6260	C	55.5180	27.6850	0.6260
C	54.6760	27.0750	1.7260	C	54.6760	27.0750	1.7260
O	55.1810	26.8990	2.8410	O	55.1810	26.8990	2.8410
C	55.4330	29.2190	0.5960	C	55.4330	29.2190	0.5960
C	54.4920	29.5670	-0.5360	C	54.4920	29.5670	-0.5360
C	54.7430	28.4600	-1.5650	C	54.7430	28.4600	-1.5650
H	56.5540	27.3900	0.7930	H	56.5540	27.3900	0.7930
H	55.0430	29.5820	1.5470	H	55.0430	29.5820	1.5470
H	56.4240	29.6370	0.4160	H	56.4240	29.6370	0.4160
H	53.4590	29.5550	-0.1860	H	53.4590	29.5550	-0.1860
H	54.7360	30.5480	-0.9420	H	54.7360	30.5480	-0.9420
H	55.5620	28.7300	-2.2320	H	55.5620	28.7300	-2.2320
N	53.4080	26.7400	1.4660	N	53.4080	26.7400	1.4660
C	52.4790	26.3020	2.5020	C	52.4790	26.3020	2.5020

C	52.0330	24.8580	2.3340	C	52.0330	24.8580	2.3340
O	51.0370	24.4400	2.9190	O	51.0370	24.4400	2.9190
C	51.2740	27.2240	2.5440	C	51.2740	27.2240	2.5440
O	50.7170	27.3190	1.2260	O	50.7170	27.3190	1.2260
C	51.6830	28.6220	3.0120	C	51.6830	28.6220	3.0120
H	52.9940	26.3650	3.4610	H	52.9940	26.3650	3.4610
H	50.5320	26.8320	3.2390	H	50.5320	26.8320	3.2390
H	50.8010	29.2550	3.1090	H	50.8010	29.2550	3.1090
H	52.1820	28.5590	3.9800	H	52.1820	28.5590	3.9800
H	52.3650	29.0720	2.2910	H	52.3650	29.0720	2.2910
H	52.9960	26.7640	0.5330	H	52.9960	26.7640	0.5330
H	49.7390	27.2880	1.2730	H	49.7390	27.2880	1.2730
N	52.7390	24.0970	1.5240	N	52.7390	24.0970	1.5240
C	52.4470	22.6650	1.3880	C	52.4470	22.6650	1.3880
C	50.9990	22.4210	0.9570	C	50.9990	22.4210	0.9570
O	50.3770	21.4340	1.3480	O	50.3770	21.4340	1.3480
C	52.8070	21.8650	2.6560	C	52.8070	21.8650	2.6560
C	54.3160	21.8370	2.9270	C	54.3160	21.8370	2.9270
O	55.1070	21.7560	1.9650	O	55.1070	21.7560	1.9650
O	54.7150	21.9010	4.1110	O	54.7150	21.9010	4.1110
H	53.0830	22.2740	0.5940	H	53.0830	22.2740	0.5940
H	52.3180	22.3220	3.5160	H	52.3180	22.3220	3.5160
H	52.4660	20.8360	2.5370	H	52.4660	20.8360	2.5370
H	53.5150	24.4280	0.9500	H	53.5150	24.4280	0.9500
N	50.4630	23.3100	0.1250	N	50.4630	23.3100	0.1250
C	48.6040	24.6120	-0.7590	C	48.6040	24.6120	-0.7590
O	48.6410	25.5010	0.3780	O	48.6410	25.5010	0.3780
H	49.2570	24.9990	-1.5420	H	49.2570	24.9990	-1.5420
H	47.5810	24.5410	-1.1290	H	47.5810	24.5410	-1.1290
H	50.9710	24.1090	-0.2530	H	50.9710	24.1090	-0.2530
H	49.5690	25.6520	0.6550	H	49.5690	25.6520	0.6550
H	53.8420	28.2580	-2.1440	H	53.8420	28.2580	-2.1440

C	54.8670	25.6480	-2.5730	C	54.8670	25.6480	-2.5730
H	55.8815	25.3859	-2.7899	H	55.8815	25.3859	-2.7899
H	54.4906	26.2860	-3.3451	H	54.4906	26.2860	-3.3451
C	49.0840	23.2390	-0.3390	C	49.0840	23.2390	-0.3390
H	48.3495	22.9463	0.3820	H	48.3495	22.9463	0.3820
H	49.1657	22.4831	-1.0919	H	49.1657	22.4831	-1.0919
C	44.1360	29.6980	-6.5540	C	44.1360	29.6980	-6.5540
O	43.3730	29.5940	-7.5270	O	43.3730	29.5940	-7.5270
C	42.7200	30.3610	-4.5900	C	42.7200	30.3610	-4.5900
C	42.4300	31.4280	-3.5210	C	42.4300	31.4280	-3.5210
C	42.9810	29.0080	-3.9420	C	42.9810	29.0080	-3.9420
C	43.5690	31.7180	-2.6010	C	43.5690	31.7180	-2.6010
H	41.8380	30.2890	-5.2260	H	41.8380	30.2890	-5.2260
H	42.1690	32.3590	-4.0230	H	42.1690	32.3590	-4.0230
H	41.5940	31.0870	-2.9100	H	41.5940	31.0870	-2.9100
H	43.1990	28.2780	-4.7210	H	43.1990	28.2780	-4.7210
H	43.8310	29.0970	-3.2660	H	43.8310	29.0970	-3.2660
H	42.0940	28.7050	-3.3860	H	42.0940	28.7050	-3.3860
H	43.1740	31.9970	-1.6240	H	43.1740	31.9970	-1.6240
H	44.1890	30.8260	-2.5100	H	44.1890	30.8260	-2.5100
H	44.1570	32.5390	-3.0120	H	44.1570	32.5390	-3.0120
N	45.1770	28.8970	-6.3650	N	45.1770	28.8970	-6.3650
C	46.9570	27.3640	-7.0720	C	46.9570	27.3640	-7.0720
H	47.1430	26.5000	-7.7100	H	47.1430	26.5000	-7.7100
H	47.6890	28.1450	-7.2800	H	47.6890	28.1450	-7.2800
H	47.0150	27.0700	-6.0240	H	47.0150	27.0700	-6.0240
H	45.7750	28.9090	-5.5390	H	45.7750	28.9090	-5.5390
C	45.5580	27.9030	-7.3610	C	45.5580	27.9030	-7.3610
H	45.5770	28.3258	-8.3437	H	45.5770	28.3258	-8.3437
H	44.7997	27.1498	-7.3114	H	44.7997	27.1498	-7.3114
C	43.9070	30.7560	-5.4800	C	43.9070	30.7560	-5.4800
H	44.8080	30.8336	-4.9080	H	44.8080	30.8336	-4.9080

H	43.6824	31.7042	-5.9221	H	43.6824	31.7042	-5.9221
C	51.9790	26.1680	-8.1830	C	51.9790	26.1682	-8.1826
S	50.4370	27.0380	-7.9180	S	50.3589	27.0411	-8.0554
H	51.7430	25.2530	-8.7260	H	51.7430	25.2530	-8.7261
H	52.3850	25.9250	-7.2010	H	52.3850	25.9249	-7.2010
C	53.0578	26.9308	-8.9741	C	53.0578	26.9307	-8.9743
H	52.7204	27.9276	-9.1674	H	52.7204	27.9276	-9.1673
H	53.9619	26.9647	-8.4028	H	53.9619	26.9647	-8.4029
H	53.2407	26.4300	-9.9018	H	53.2407	26.4300	-9.9019

Part 2. **CM_H** model

Before optimization				After optimization			
Fe	51.1560	26.9070	-3.1790	Fe	51.0943	26.8246	-3.0613
Fe	48.9800	28.4489	-3.5851	Fe	48.9111	28.3918	-3.6611
Fe	50.4430	27.5580	-5.7080	Fe	50.4148	27.5566	-5.7999
Fe	51.4720	29.4670	-3.9990	Fe	51.5223	29.5247	-4.0565
S	49.6810	29.6960	-5.3490	S	49.6625	29.7604	-5.4967
S	52.5230	27.6210	-4.8270	S	52.5387	27.4961	-4.9493
S	50.5580	28.7750	-2.0490	S	50.4679	28.8805	-2.0194
S	49.2930	26.3130	-4.2320	S	49.2421	26.1403	-4.3041
N	48.0580	30.4920	-0.2770	N	48.0580	30.4920	-0.2770
C	48.2190	31.9190	-0.0090	C	48.2190	31.9190	-0.0090
C	48.3730	32.7390	-1.2940	C	48.3730	32.7390	-1.2940
O	48.7900	33.8980	-1.2400	O	48.7900	33.8980	-1.2400
C	49.3620	32.1790	0.9940	C	49.3620	32.1790	0.9940
C	50.6630	31.5940	0.4580	C	50.6630	31.5940	0.4580
C	49.0440	31.5800	2.3410	C	49.0440	31.5800	2.3410
C	51.9050	32.0390	1.2310	C	51.9050	32.0390	1.2310
H	47.2970	32.2680	0.4560	H	47.2970	32.2680	0.4560
H	49.4700	33.2570	1.1130	H	49.4700	33.2570	1.1130

H	50.6080	30.5060	0.5150	H	50.6080	30.5060	0.5150
H	50.7880	31.9070	-0.5790	H	50.7880	31.9070	-0.5790
H	49.8510	31.8180	3.0350	H	49.8510	31.8180	3.0350
H	48.1060	32.0000	2.7040	H	48.1060	32.0000	2.7040
H	48.9520	30.4990	2.2370	H	48.9520	30.4990	2.2370
H	51.9350	31.5140	2.1860	H	51.9350	31.5140	2.1860
H	52.7920	31.7970	0.6470	H	52.7920	31.7970	0.6470
H	51.8510	33.1140	1.3990	H	51.8510	33.1140	1.3990
H	48.9190	30.0350	-0.5770	H	48.9190	30.0350	-0.5770
N	48.0060	32.1770	-2.4590	N	48.0060	32.1770	-2.4590
C	47.9220	32.9400	-3.7090	C	47.9220	32.9400	-3.7090
C	49.2490	33.5790	-4.1010	C	49.2490	33.5790	-4.1010
O	49.2890	34.7350	-4.5340	O	49.2890	34.7350	-4.5340
C	46.8110	33.9910	-3.6580	C	46.8110	33.9910	-3.6580
H	47.0150	34.6840	-2.8420	H	47.0150	34.6840	-2.8420
H	46.7870	34.5300	-4.6050	H	46.7870	34.5300	-4.6050
H	45.8560	33.4920	-3.4910	H	45.8560	33.4920	-3.4910
H	47.7610	31.1920	-2.5620	H	47.7610	31.1920	-2.5620
N	50.3390	32.8210	-3.9700	N	50.3390	32.8210	-3.9700
C	51.6820	33.3450	-4.1880	C	51.6820	33.3451	-4.1880
C	52.1330	33.3380	-5.6420	C	52.1330	33.3380	-5.6420
O	53.1130	34.0180	-5.9580	O	53.1130	34.0180	-5.9580
C	52.6910	32.5740	-3.3400	C	52.6908	32.5738	-3.3400
S	53.1610	30.9800	-3.9860	S	53.2990	30.9481	-3.9670
H	51.6800	34.3870	-3.8670	H	51.6800	34.3870	-3.8670
H	53.5990	33.1720	-3.2550	H	53.5990	33.1720	-3.2550
H	52.2580	32.4120	-2.3530	H	52.2581	32.4121	-2.3530
H	50.3230	31.8340	-3.7130	H	50.3230	31.8340	-3.7130
N	51.4710	32.5970	-6.5310	N	51.4710	32.5970	-6.5310
C	51.8280	32.5970	-7.9410	C	51.8280	32.5970	-7.9410
C	52.9710	31.6780	-8.3700	C	52.9710	31.6780	-8.3700
O	53.2910	31.6460	-9.5690	O	53.2910	31.6460	-9.5690

H	50.9480	32.3030	-8.5130	H	50.9480	32.3030	-8.5130
H	52.1100	33.6120	-8.2200	H	52.1100	33.6120	-8.2200
H	50.6850	31.9900	-6.3000	H	50.6850	31.9900	-6.3000
N	53.5830	30.9120	-7.4580	N	53.5830	30.9120	-7.4580
C	55.4720	29.6470	-6.5520	C	55.4720	29.6470	-6.5520
H	55.9630	30.5010	-6.0850	H	55.9630	30.5010	-6.0850
H	54.7450	29.2140	-5.8650	H	54.7450	29.2140	-5.8650
H	56.2140	28.8970	-6.8290	H	56.2140	28.8970	-6.8290
H	53.2970	30.8250	-6.4830	H	53.2970	30.8250	-6.4830
C	46.8895	29.8555	-0.1395	C	46.8895	29.8555	-0.1395
H	47.6780	32.2250	-4.4950	H	47.6780	32.2250	-4.4950
S	46.8110	29.0760	-3.1900	S	46.7475	29.1063	-3.2748
C	46.2315	28.0983	-1.8201	C	46.2318	28.0982	-1.8202
H	45.4454	28.6209	-1.3162	H	45.4454	28.6209	-1.3163
H	45.8624	27.1613	-2.1815	H	45.8623	27.1613	-2.1815
O	45.8590	30.4070	0.2360	O	45.8590	30.4070	0.2360
C	46.9000	28.3700	-0.4560	C	46.8999	28.3701	-0.4560
H	46.3416	27.6187	0.0623	H	46.3415	27.6187	0.0623
H	47.9403	28.2600	-0.2310	H	47.9403	28.2599	-0.2310
C	54.7490	30.1170	-7.8080	C	54.7490	30.1170	-7.8080
H	55.5724	30.5645	-8.3243	H	55.5724	30.5645	-8.3244
H	54.2481	29.4329	-8.4607	H	54.2481	29.4329	-8.4607
C	55.1890	26.0230	-1.1240	C	55.1890	26.0230	-1.1240
O	55.4750	25.1350	-0.3250	O	55.4750	25.1350	-0.3250
C	53.6470	24.7440	-2.6300	C	53.6469	24.7441	-2.6301
S	52.2130	25.4380	-1.7640	S	52.2521	25.4563	-1.6763
H	53.3690	24.5900	-3.6730	H	53.3690	24.5900	-3.6730
H	53.8920	23.7890	-2.1650	H	53.8920	23.7890	-2.1650
N	55.1020	27.3040	-0.7420	N	55.1020	27.3040	-0.7420
C	55.5180	27.6850	0.6260	C	55.5180	27.6850	0.6260
C	54.6760	27.0750	1.7260	C	54.6760	27.0750	1.7260
O	55.1810	26.8990	2.8410	O	55.1810	26.8990	2.8410

C	55.4330	29.2190	0.5960	C	55.4330	29.2190	0.5960
C	54.4920	29.5670	-0.5360	C	54.4920	29.5670	-0.5360
C	54.7430	28.4600	-1.5650	C	54.7430	28.4600	-1.5650
H	56.5540	27.3900	0.7930	H	56.5540	27.3900	0.7930
H	55.0430	29.5820	1.5470	H	55.0430	29.5820	1.5470
H	56.4240	29.6370	0.4160	H	56.4240	29.6370	0.4160
H	53.4590	29.5550	-0.1860	H	53.4590	29.5550	-0.1860
H	54.7360	30.5480	-0.9420	H	54.7360	30.5480	-0.9420
H	55.5620	28.7300	-2.2320	H	55.5620	28.7300	-2.2320
N	53.4080	26.7400	1.4660	N	53.4080	26.7400	1.4660
C	52.4790	26.3020	2.5020	C	52.4790	26.3020	2.5020
C	52.0330	24.8580	2.3340	C	52.0330	24.8580	2.3340
O	51.0370	24.4400	2.9190	O	51.0370	24.4400	2.9190
C	51.2740	27.2240	2.5440	C	51.2740	27.2240	2.5440
O	50.7170	27.3190	1.2260	O	50.7170	27.3190	1.2260
C	51.6830	28.6220	3.0120	C	51.6830	28.6220	3.0120
H	52.9940	26.3650	3.4610	H	52.9940	26.3650	3.4610
H	50.5320	26.8320	3.2390	H	50.5320	26.8320	3.2390
H	50.8010	29.2550	3.1090	H	50.8010	29.2550	3.1090
H	52.1820	28.5590	3.9800	H	52.1820	28.5590	3.9800
H	52.3650	29.0720	2.2910	H	52.3650	29.0720	2.2910
H	52.9960	26.7640	0.5330	H	52.9960	26.7640	0.5330
H	49.7390	27.2880	1.2730	H	49.7390	27.2880	1.2730
N	52.7390	24.0970	1.5240	N	52.7390	24.0970	1.5240
C	52.4470	22.6650	1.3880	C	52.4470	22.6650	1.3880
C	50.9990	22.4210	0.9570	C	50.9990	22.4210	0.9570
O	50.3770	21.4340	1.3480	O	50.3770	21.4340	1.3480
C	52.8070	21.8650	2.6560	C	52.8070	21.8650	2.6560
C	54.3160	21.8370	2.9270	C	54.3160	21.8370	2.9270
O	55.1070	21.7560	1.9650	O	55.1070	21.7560	1.9650
H	53.0830	22.2740	0.5940	H	53.0830	22.2740	0.5940
H	52.3180	22.3220	3.5160	H	52.3180	22.3220	3.5160

H	52.4660	20.8360	2.5370	H	52.4660	20.8360	2.5370
H	53.5150	24.4280	0.9500	H	53.5150	24.4280	0.9500
N	50.4630	23.3100	0.1250	N	50.4630	23.3100	0.1250
C	48.6040	24.6120	-0.7590	C	48.6040	24.6120	-0.7590
O	48.6410	25.5010	0.3780	O	48.6410	25.5010	0.3780
H	49.2570	24.9990	-1.5420	H	49.2570	24.9990	-1.5420
H	47.5810	24.5410	-1.1290	H	47.5810	24.5410	-1.1290
H	50.9710	24.1090	-0.2530	H	50.9710	24.1090	-0.2530
H	49.5690	25.6520	0.6550	H	49.5690	25.6520	0.6550
H	53.8420	28.2580	-2.1440	H	53.8420	28.2580	-2.1440
C	54.8670	25.6480	-2.5730	C	54.8670	25.6480	-2.5730
H	55.8815	25.3859	-2.7899	H	55.8815	25.3859	-2.7899
H	54.4906	26.2860	-3.3451	H	54.4906	26.2860	-3.3451
C	49.0840	23.2390	-0.3390	C	49.0840	23.2390	-0.3390
H	48.3495	22.9463	0.3820	H	48.3495	22.9463	0.3820
H	49.1657	22.4831	-1.0919	H	49.1657	22.4831	-1.0919
O	54.7173	21.9014	4.1179	O	54.7173	21.9014	4.1179
H	55.6962	21.9043	4.0821	H	55.6962	21.9043	4.0821
C	44.1360	29.6980	-6.5540	C	44.1360	29.6980	-6.5540
O	43.3730	29.5940	-7.5270	O	43.3730	29.5940	-7.5270
C	42.7200	30.3610	-4.5900	C	42.7200	30.3610	-4.5900
C	42.4300	31.4280	-3.5210	C	42.4300	31.4280	-3.5210
C	42.9810	29.0080	-3.9420	C	42.9810	29.0080	-3.9420
C	43.5690	31.7180	-2.6010	C	43.5690	31.7180	-2.6010
H	41.8380	30.2890	-5.2260	H	41.8380	30.2890	-5.2260
H	42.1690	32.3590	-4.0230	H	42.1690	32.3590	-4.0230
H	41.5940	31.0870	-2.9100	H	41.5940	31.0870	-2.9100
H	43.1990	28.2780	-4.7210	H	43.1990	28.2780	-4.7210
H	43.8310	29.0970	-3.2660	H	43.8310	29.0970	-3.2660
H	42.0940	28.7050	-3.3860	H	42.0940	28.7050	-3.3860
H	43.1740	31.9970	-1.6240	H	43.1740	31.9970	-1.6240
H	44.1890	30.8260	-2.5100	H	44.1890	30.8260	-2.5100

H	44.1570	32.5390	-3.0120	H	44.1570	32.5390	-3.0120
N	45.1770	28.8970	-6.3650	N	45.1770	28.8970	-6.3650
C	46.9570	27.3640	-7.0720	C	46.9570	27.3640	-7.0720
H	47.1430	26.5000	-7.7100	H	47.1430	26.5000	-7.7100
H	47.6890	28.1450	-7.2800	H	47.6890	28.1450	-7.2800
H	47.0150	27.0700	-6.0240	H	47.0150	27.0700	-6.0240
H	45.7750	28.9090	-5.5390	H	45.7750	28.9090	-5.5390
C	45.5580	27.9030	-7.3610	C	45.5580	27.9030	-7.3610
H	45.5771	28.3258	-8.3437	H	45.5771	28.3258	-8.3437
H	44.7997	27.1498	-7.3114	H	44.7997	27.1498	-7.3114
C	43.9070	30.7560	-5.4800	C	43.9070	30.7560	-5.4800
H	44.8080	30.8336	-4.9080	H	44.8080	30.8336	-4.9080
H	43.6824	31.7042	-5.9221	H	43.6824	31.7042	-5.9221
C	51.9790	26.1680	-8.1830	C	51.9790	26.1682	-8.1827
S	50.4370	27.0380	-7.9180	S	50.3626	27.0425	-8.0337
H	51.7430	25.2530	-8.7260	H	51.7430	25.2530	-8.7260
H	52.3850	25.9250	-7.2010	H	52.3850	25.9249	-7.2010
C	53.0578	26.9308	-8.9741	C	53.0578	26.9307	-8.9743
H	52.7204	27.9276	-9.1674	H	52.7204	27.9276	-9.1674
H	53.9619	26.9647	-8.4028	H	53.9619	26.9647	-8.4029
H	53.2408	26.4300	-9.9018	H	53.2407	26.4300	-9.9019

Table S4. Calculated IP values of the CM_H and CM models with and without the environment effect.

	IP(red) values	
	Gas phase	IEFPCM (Eps=4) (*7*)
CM_H	–1.06	2.59
CM	–3.27	1.62
ΔIP	2.21	0.97

Table S5. The distance between the acidic residues and the [4Fe-4S] cluster.*

		Distance between the Cγ of Asp and the [4Fe-4S] cluster, (Å)	Remarks
D7		10.5	
D23		16.6	
D26		12.0	
D28		11.3	
D30		13.7	
D38		16.2	
D39		16.9	
D48		24.0	
D52		19.2	
D53		15.1	
D56		13.7	
D64		10.1	
D70		23.0	
D74		22.4	
D76		18.2	

		Distance(s) between the Cδ of Glu and the [4Fe-4S] cluster, (Å)	Remarks
E9		13.0	
E45		22.4 21.7	Alternative conformations
E59		12.8	
E71		23.4 22.9 22.2	Alternative conformations
E81		16.4	

* Distances are shown by measuring the center-of-gravity coordinates of the [4Fe-4S] cluster and the sidechain terminal carbon of acidic residues.

References

1. F. Delaglio *et al.*, NMRPipe: a multidimensional spectral processing system based on UNIX pipes. *J Biomol NMR* **6**, 277-293 (1995).
2. W. Lee, M. Tonelli, J. L. Markley, NMRFAM-SPARKY: enhanced software for biomolecular NMR spectroscopy. *Bioinformatics* **31**, 1325-1327 (2015).
3. M. Sattler, J. Schleucher, C. Griesinger, Heteronuclear multidimensional NMR experiments for the structure determination of proteins in solution employing pulsed field gradients. *Progress in Nuclear Magnetic Resonance Spectroscopy* **34**, 93-158 (1999).
4. R. T. Clowes, W. Boucher, C. H. Hardman, P. J. Domaille, E. D. Laue, A 4D HCC(CO)NNH experiment for the correlation of aliphatic side-chain and backbone resonances in 13C/15N-labelled proteins. *Journal of Biomolecular NMR* **3**, 349-354 (1993).
5. M. Kostic, S. S. Pochapsky, T. C. Pochapsky, Rapid Recycle 13C‘,15N and 13C,13C‘ Heteronuclear and Homonuclear Multiple Quantum Coherence Detection for Resonance Assignments in Paramagnetic Proteins: Example of Ni2+-Containing Acireductone Dioxygenase. *Journal of the American Chemical Society* **124**, 9054-9055 (2002).
6. J. Ying, F. Li, J. H. Lee, A. Bax, ^{13}Calpha decoupling during direct observation of carbonyl resonances in solution NMR of isotopically enriched proteins. *J Biomol NMR* **60**, 15-21 (2014).
7. L. Li, C. Li, Z. Zhang, E. Alexov, On the Dielectric "Constant" of Proteins: Smooth Dielectric Function for Macromolecular Modeling and Its Implementation in DelPhi. *J Chem Theory Comput* **9**, 2126-2136 (2013).